Copyright Warning & Restrictions

The copyright law of the United States (Title 17, United States Code) governs the making of photocopies or other reproductions of copyrighted material.

Under certain conditions specified in the law, libraries and archives are authorized to furnish a photocopy or other reproduction. One of these specified conditions is that the photocopy or reproduction is not to be "used for any purpose other than private study, scholarship, or research." If a, user makes a request for, or later uses, a photocopy or reproduction for purposes in excess of "fair use" that user may be liable for copyright infringement,

This institution reserves the right to refuse to accept a copying order if, in its judgment, fulfillment of the order would involve violation of copyright law.

Please Note: The author retains the copyright while the New Jersey Institute of Technology reserves the right to distribute this thesis or dissertation

Printing note: If you do not wish to print this page, then select "Pages from: first page # to: last page #" on the print dialog screen

NJIT
New Jersey's Science & Technology University

The Van Houten library has removed some of the personal information and all signatures from the approval page and biographical sketches of theses and dissertations in order to protect the identity of NJIT graduates and faculty.

ABSTRACT

CHARACTERIZATION OF α AND β PHASES OF TANTALUM COATINGS

by
Anto Yohannan

Sputtered tantalum forms two phases - α and β. The α and β phases have distinctly different crystalline structures and properties. The structure and the causes of formation of the β phase are still being studied by researchers. This is a study to distinguish and characterize these two phases. Samples from Bennet Labs and NJIT were characterized using techniques such as SEM, EDX, XRF, XRD, TEM and XAFS. Samples deposited at NJIT were used for an experimental study on the conditions favoring the formation of the phases, by depositing tantalum on heated steel and silicon substrates, additionally TEM analysis was carried out for a sample having a mixture of α and β phases to study its differences. The XRD results shows one of the sample to be highly textured β Tantalum. The XAFS results also show the α phase to have a bcc structure with the characterstic coordination of bulk tantalum.The local structure of β tantalum is compared to a theoretical model of P4/*mnm* space group. The study confirm that the structure of β tantalum belongs to this space group and has a 30-atom unit cell isomorphous with β Uranium. The coordination of Ta atoms in the β phase is seen to be non isotropic. The results of the heating experiments suggest that coatings deposited on substrates without heating favored the formation of the β phase. The TEM analysis shows the β phase to be made up of larger grains of size 100-120 nm, which are about 4 times the size of the α phase grains.

CHARACTERIZATION OF α AND β PHASES OF TANTALUM COATINGS

by
Anto Yohannan

A Thesis
Submitted to the Faculty of
New Jersey Institute of Technology
in partial fulfillment of the requirements for the Degree of
Master of Science in Materials Science and Engineering

Department of Materials Science and Engineering
August 2001

APPROVAL PAGE

CHARACTERIZATION OF α AND β PHASES OF TANTALUM COATINGS

Anto Yohannan

Dr. Trevor Tyson, Thesis Adviser — Date
Associate Professor of Physics, NJIT

Dr. Marek Sosnowski, Committee Member — Date
Associate Professor of ECE, NJIT

Dr. Lisa Axe, Committee Member — Date
Associate Professor of Civil and Environmental Engineering, NJIT

BIOGRAPHICAL SKETCH

Author: Anto Yohannan

Degree: Master of Science

Date: August 2001

Undergraduate and Graduate Education:

- Master of Science in Materials Science and Engineering
  New Jersey Institute of Technology, Newark, NJ, 2001

- Bachelor of Mechanical Engineering
  Osmania University, Hyderabad, India, 1990

Major: Materials Science and Engineering

Dedicated to Mama and Papa, who are my inspiration

..... If you can make one heap of all your winnings
And risk it all on one turn of pitch-and-toss,
And lose, and start again at your beginnings
And never breath a word about your loss;
If you can force your heart and nerve and sinew
To serve your turn long after they are gone,
And so hold on when there is nothing in you
Except the Will which says to them: "Hold on!"

...... Yours is the Earth and everything that's in it,
And--which is more--you'll be a Man, my son!

--Rudyard Kipling

and to my wife Dolly and son Nikki mon, for being patient

ACKNOWLEDGEMENT

I would like to express my sincere gratitude to my adviser, Dr Trevor Tyson, for his guidance and support throughout this research. I also thank Dr Lisa Axe and Dr Marek Sosnowski not only for their inputs as members of my committee but also for their guidance during this research.

I thank the Sustainable Green Manufacturing Program of the US Army, and Dr Daniel Watts for providing the research assistantship to pursue my graduate studies. I am also grateful to Dr Paul Cote (Bennet Labs, Watevilet), Anamika Patel and Bhavin Shah (Dr. Sosnowski's group at NJIT) for providing me with the samples for this work. I am thankful to Dr Sabrina Lee (Bennet Labs, Watevilet) for her inputs and research reports, which helped me in this research. I also express my gratitude to Keith Wagner (RG Lee Group) for the transmission electron microscopy work.

I acknowledge, the contribution of Neme Nnolim, Sungmin Maeng and Aiqin Jiang without whose help and cooperation this work would have remained incomplete. Finally, with deep gratitude, I thank my parents, in-laws and my wife, Rossa for their love and patience during my master's degree study.

TABLE OF CONTENTS

Chapter **Page**

1 INTRODUCTION

1.1 Objective 1

1.2 Background 3

1.3 Scope of Work 8

2 PHYSICAL VAPOR DEPOSITION

2.1 Introduction 9

2.2 DC diode sputtering system 9

2.3 Magnetron sputtering 11

2.4 Process considerations that affect film characteristics 14

2.5 Literature review 16

2.5.1 Film Purity 16

2.5.2 Effect of Substrate 16

2.5.3 Effect of Underlayers 17

2.5.4 Effect of Sputter Gas 18

2.5.5 Substrate Bias 19

2.5.6 Substrate Temperature 20

3 CHARACTERIZATION TECHNIQUES

3.1 X-ray Diffraction 22

3.1.1 Introduction 22

3.2.1 Description 22

3.2 Scanning Electron Microscope 24

TABLE OF CONTENTS

(continued)

Chapter Page

3.1.1 Introduction 24

3.2.1 Description 24

3.3 Energy Dispersive X-ray Spectroscopy 27

3.1.1 Introduction 27

3.2.1 Description 27

3.4 X-ray Fluorescence Spectroscopy 28

3.1.1 Introduction 28

3.2.1 Description 28

3.5 X-ray Absorption Spectroscopy 30

3.1.1 Introduction 30

3.2.1 Description 31

3.6 Transmission Electron Microscopy 33

3.1.1 Introduction 33

3.2.1 Description 33

4 TANTALUM DEPOSITION

4.1 Introduction 38

4.2 Deposition Process 38

4.2.1 TEM Sample Preparation 41

TABLE OF CONTENTS

(continued)

Chapter **Page**

5 ANALYSIS OF SAMPLES

5.1 Introduction 43

5.2 X-ray Diffraction Analysis 43

5.3 X-ray Fluorescence 51

5.4 Energy Dispersive X-ray Spectroscopy 52

5.5 Scanning Electron Microscope 53

5.6 Extended X-ray Absorption Spectroscopy 56

5.7 TEM Analysis 66

6 DISCUSSION

6.1 X-ray Diffraction Analysis 71

6.2 X-ray Fluorescence & EDX 74

6.3 Scanning Electron Microscope 75

6.4 Transmission Electron Microscopy 76

6.5 X-ray Absorption Spectroscopy 77

6.6 Discussion on heated Substrates 78

7 CONCLUSIONS 80

APPENDIX A Different modes of XAFS Experiments 81

APPENDIX B Coordinates of β Tantalum structure 83

APPENDIX C Structure Factor calculations 84

REFERENCES 87

LIST OF FIGURES

Figure		Page
2.1	DC diode sputtering system	11
2.2	Magnetron sputtering	13
3.1	Schematic of XRD set up	23
3.2	Schematic of SEM set up	25
3.3	Schematic of XRF set up	29
3.4	Schematic of XAFS set up	30
3.5	Schematic of TEM set up	34
4.1	Schematic of Sputtering System	40
5.1	X-ray Scan of Ta Powder	45
5.2	X-ray Scan of Sample A	46
5.3	X-ray Scan of Sample B	47
5.4	X-ray Scan of Sample C & D	48
5.5	X-ray Scan of Sample E & F	49
5.6	X-ray Scan of Sample G	50
5.7	EDX spectrum of Sample A & B	52
5.8	SEM of Sample A	54
5.9	SEM of Sample B	55
5.10	$\chi(\kappa)\kappa^3$ data for Theoretical model of β & α Ta	58
5.11	$\chi(\kappa)\kappa^3$ experimental data for sample A and B	59
5.12	Fourier Transforms for Theoretical data	60

LIST OF FIGURES

(continued)

Figure **Page**

5.13 Fourier Transforms for Experimental data 61

5.14 Comparison of χ (κ) κ^3 data for diferent modes of β Ta 62

5.15 Comparison of Fourier data for diferent modes of β Ta 63

5.16 χ (κ) κ^3 data at 45° & calculated 0 & 90° for β Ta 64

5.17 Fourier transforms data at 45° & calculated 0 & 90° for β Ta 65

5.18 TEM image of Sample G showing α Ta 67

5.19 TEM image of Sample G showing β Ta 68

5.20 Electron Diffraction pattern of Sample G showing α Ta 69

5.21 Electron Diffraction pattern of Sample G showing β Ta 70

6.1 Main Crsytal Planes of β & α Ta 73

A1 Schematic of XAFS experiment at 45° 81

A2 Schematic of XAFS experiment at 45° 81

A3 Schematic of XAFS experiment at 45° 82

LIST OF TABLES

Table		Page
1.1	Properties of Ta and Cr	2
1.2	Properties of Bulk ta, α & β ta	4
1.3	Structural Studies of β ta	7
4.1	Details of Samples used in this study	39
5.1	Details of Characterisation Techniques used	43
5.2	XRF results of the Samples	51
6.1	Composition of Impurities in the two phases	75
6.2	Grain sizes of the two phases determined by Researchers	77

CHAPTER 1

INTRODUCTION

1.1 Objective

Sputtered films of tantalum are being investigated to replace chromium coatings in the bores of gun barrels, because of their superior high temperature corrosion-erosion resistant properties. Tantalum coatings are found to have two distinct phases- α and β. The α phase has better corrosion resistance properties than the β phase and is therefore the preferred phase of tantalum for this application. Gun barrels are made of low alloy steels that typically have 96-97% iron and the rest composed mainly of alloying elements nickel, chromium and molybdenum [1]. It has a melting point of about 1400 °C. During firing the barrel surface is subjected to the propellant chemicals and mechanical stresses at temperatures nearing its melting point. This results in progressive corrosion and erosion at the bore surfaces and thus decreases their productive use. To increase their life electroplated chromium coatings are currently used as a resistant liner. However, chromium is brittle and thus can crack with frequent use. It is also, toxic and an environmental hazard [2]. Hence, research is being done on newer coatings to replace chromium as the corrosion resistant coating on the gun barrel steels. As a highly stable refractory metal, tantalum is chosen for these studies because of its high melting point, resistance to most chemicals and low toxicity [3]. Tantalum is a dark silvery gray metal in appearance and is highly resistant to most commercial acids. A few important properties of tantalum and chromium are compared in Table 1.1 [2].

Table 1.1, Properties of Tantalum and Chromium

Properties	Chromium	Tantalum
Melting point °C	1875	2996
Coefficient of thermal expansion µm/m K at 20 °C	6.2	6.5
Thermal Conductivity at 20 °C in W/m K	67	54.4
Tensile Strength MPa at 20 °C	83	325
Density mg/m^3 at 20 °C	7.19	16.6

Tantalum coatings also, have many other commercial applications especially in the electronics industry [20, 22, 23, 27, 36, 37,59,60,61]. It is used as thin film resistors and as absorbers in X-ray lithography. In semiconductors, the advent of copper interconnects for deep sub micron multilevel integrated circuits (ICs), has led to research on tantalum coatings. Tantalum is one of the most promising barriers to prevent the highly diffusing copper from reacting with the underlying silicon. Oxides and nitrides of tantalum are also, being investigated for these applications. For electrical applications, thin films of α tantalum are preferred because their resistivity is substantially lower than β tantalum.

Three different processes can be used to apply tantalum coatings – electrodeposition from fused salts [4,5], chemical vapor deposition [6] and physical vapor deposition. The elecrodeposition process requires a deposition temperature of

about 800 °C. However, the gun barrels cannot be exposed to such high temperatures as this could lead to irreversible phase changes in the steel and also, affect its mechanical properties thereby reducing its life [7]. Chemical vapor deposition also, cannot be used for the same reasons. The sputtering process does not increase the substrate temperature beyond 400 °C, and a suitable sputtering system can be developed to uniformly coat tantalum on the bores of the barrels. Therefore sputtering is the most appropriate process for this application.

1.2 Background

Sputtered films of tantalum are found to have two different and unique structures, a stable α phase and a metastable β tantalum [8]. While the α phase was found to have properties similar to that of bulk tantalum and had a body centered cubic structure, studies to determine the structure of the β phase and reasons for formation are still being investigated. α phase possesses good chemical, thermal and mechanical properties, good ductility and formability, and resistance to aggressive hot propellant gases [9, 29, 30]. While the β phase is hard, brittle and thermally unstable. β Tantalum transforms to α tantalum when heated to temperatures between 750 and 900°C [8] .The properties of the α and β phase are tabulated in Table 1.2 [8].

The two structures of tantalum and their formation have been studied from the nineteen sixties. Researchers have reported different lattice constants for β tantalum based on their studies. Table 1.3 lists the work conducted done on the crystal structure of β tantalum. Studies done on process controls for obtaining the α or the β phase is discussed in Chapter 2.

Table 1.2, Properties of bulk, α and β tantalum

Properties	Bulk tantalum	α phase	β phase
Structure	Body centered	Body centered	Tetragonal
Density g cm^{-3}	16.655	16.55	16.9
Resistivity μ -ohm-cm	13	24-50	180-220
Temperature coef. of resistivity ppm/ °C	+3800	+500 +1800	-100 +100
Superconductivity °K	4.4	3.25	0.5

Read and Altman [8] investigated the β phase and observed that high vacuum and low concentration of residual gases favored the formation of this phase. This phase was indexed as a tetragonal structure having lattice constants a = 5.34 Å and c = 9.94 Å. It was also, found to have a distinct orientation relative to the substrate, which was the same irrespective of the crystalline nature of the substrate. A wide film X-ray camera was used for the study. β tantalum was observed to have a fiber texture. Das [10] proposed a bcc-based superlattice unit cell, which was slightly distorted cubic, based on the study using transmission electron microscopy. Tantalum films, approximately 2000 Å thick, deposited on thermally oxidized, silicon single crystal substrates were used for

this work[10]. This study also, compared this superlattice model with that of Ta-N which has a 27 atom superlattice unit cell. Based on results of electron diffraction analysis, the β tantalum structure was found to belong to the P*4/mmm* space group.

Mills [11] studied the deposition of Tantalum films on different substrates and studied the crystal structures of β and α Tantalum. While Burbank [12] proposed a hexagonal sub cell for β tantalum based on the study of using β tantalum flakes. β Tantalum flakes for this X-ray study were obtained from a film of 7.5 μm thickness that had been separated from the substrate and was available as small flakes. Two types of diffraction experiments were performed. The Gandolfi technique was used for experimental elimination of the effects of preferred orientation, while another technique was used to make maximum use of the preferred orientation for its single – crystal- like structure. The smallest hexagonal cell that accounted for all the observed spacings contained 144 hexagonal sub cells with a = 34 Å. It was suggested that the structure had domains in the form of hexagonal prisms about 1000 Å in height and 250 Å in diameter.

Moseley et al. [4] indexed the powder pattern of electrodeposited β tantalum in terms of a tetragonal unit cell. β Tantalum was prepared as a single phase by elecrodeposition from a molten fluoride bath at 800 °C. The X-ray powder method was recorded for this sample using a Nonius Guinier camera calibrated against silicon standard. The structure of β tantalum was found to be isomorphous with β uranium and was postulated to have a thirty-atom unit cell. The β phase was also, observed to transform irreversibly to the α phase upon heating to 1000 °C.

Thompson [5] reported different lattice constants for β tantalum in his study of electrodeposited tantalum on copper. β tantalum deposited to a thickness exceeding 3 mils from a eutectic mixture of LiF.NaF.KF (FLINAK) molten salt electrolyte on copper was used for these experiments. The coatings were observed to have a preferred orientation. The structural studies of researchers are tabulated in Table 1.3.

Table 1.3 Structural studies of β tantalum

	Structure	Lattice constants Å	Substrate
Read and Altman [8]	Tetragonal	a = 5.34, c = 9.94	No specific substrate mentioned
Mills [11]	Tetragonal	a = 5.32, c = 9.92	Aluminoborosilicate Glass, Quartz
Das [10]	Tetragonal	a = 10.29, c = 9.2	Thermally oxidized silicon
Burbank [12]	Hexagonal subcell	a = 2.831, c = 5.337	Not mentioned, β Ta flakes used
Moseley [4]	Tetragonal	a = 10.194, c = 5.313	Electrodeposition process
Thompson [5]	Tetragonal	a = 5.34, c = 3.051	Electrodeposited on copper substrate

1.3 Scope of Work

This is a study to identify and distinguish the two Ta phases and their properties; an attempt is also, made to determine the possible local structure for β tantalum. Characterization techniques used included X-ray diffraction (XRD), Transmission Electron Microscopy (TEM), Scanning electron microscope (SEM), Energy Dispersive X-ray (EDX), X-ray fluorescence (XRF) and X-ray absorption fine structure spectroscopy (EXAFS). XRD helped to identify the formed phases and their preferred orientations based on their diffraction peaks. The elemental composition was determined using EDX and XRF techniques. SEM was used to determine and compare the surface morphology while EXAFS was used to study the local structures of the two phases. TEM was used to study and compare the grain structures of α and β tantalum. The samples used in this study are tabulated in Table 4.1, chapter 4.Bennett laboratory [64] and NJIT provided the samples for this study. The affect of substrate heating in the formation of the phases was studied on NJIT samples. This experiment [65] compares the phase formed on heated and unheated steel and silicon substrates, samples C, D,E and F. β Tantalum is seen to be more predominant on substrates that are not heated. This shows that the formation of the phases is dependent on the condition of the substrate surface. Transmission Electron Microscopy (TEM) analysis was carried out for sample G having 90 % β tantalum for its characterization study [65]. Two areas from the same sample were analyzed. The TEM image shows α tantalum having a fine grain structure. β tantalum is observed to be of a larger grain size than α.

CHAPTER 2

PHYSICAL VAPOR DEPOSITION

2.1 Introduction

Thin films using PVD are prepared by condensation of atoms or molecules impinging onto the substrate. PVD includes evaporation and sputtering processes [14]. In evaporation, atoms are removed from the source thermally, whereas in sputtering the atoms are dislodged from a solid target by the impact of gaseous ions. The advances in vacuum pumping equipment and Joule heating sources spurred emergence of PVD as a suitable industrial film deposition process. Sputtering displaced evaporation as it had numerous distinct advantages. These included – alloy deposition, composition of which can be more tightly controlled, control of film properties such as step coverage and variation of electrical parameters to control grain structure. Also, unlike evaporation, where the crucible must be horizontal and placed vertically below the substrate, sputtering is possible with the source in any orientation, provided it faces the substrate. The simplest sputtering systems are the dc diode and dc magnetron systems, which have been used in the majority of the studies on tantalum coatings.

2.2 DC Diode Sputtering System

In general, the sputtering process consists of four steps. Ions are generated and directed at a target. The ions sputter target atoms. The ejected atoms are transported to the substrate. Upon reaching the substrate, they condense and form a thin film. The energetic ions used to strike the target are generated by glow discharges.

The target is a plate of the material to be deposited. It is the cathode and the substrate that faces this electrode, and may be grounded, electrically floating, biased positively or negatively. The system is confined in a chamber, which is evacuated to vacuum. After evacuation of the chamber, a gas typically argon, is introduced and serves as the medium in which a discharge is initiated and sustained. Gas pressures usually range upto few hundreds of millitorr. Initial application of voltage between the electrodes produces a very small current due to the small number of initial charge carriers in the system. As the voltage is increased, sufficient energy is imparted to the charge particles to create more carriers. This occurs through ion collisions with the cathode, which release secondary electrons, and by electron impact ionization of neutral gas atoms. With charge multiplication, the current increases rapidly. The gas begins to glow at this point, and the voltage drops accompanied by a sharp rise in current. Eventually, when enough of the electrons generated produce sufficient ions to regenerate the same number of initial electrons, the discharge becomes self-sustaining. Plasma is defined as a partially ionized gas containing an equal number of positive and negative charges as well as neutral gas particles.

In application such as plasma enhanced chemical vapor deposition (PECVD) or reactive ion etching (RIE) it is this plasma which allows for reactions to take place at lower temperatures which otherwise would have required very high temperatures. Figure 2.1 [14] is a schematic of a simple dc diode system. DC power supplies are used for sputtering with targets that conduct electricity and can dissipate the surface charge induced by the bombarding ions. RF power is used for poorly conducting and insulating

targets, which quickly build a surface charge in opposition to the applied potential if sputtered with DC power supply.

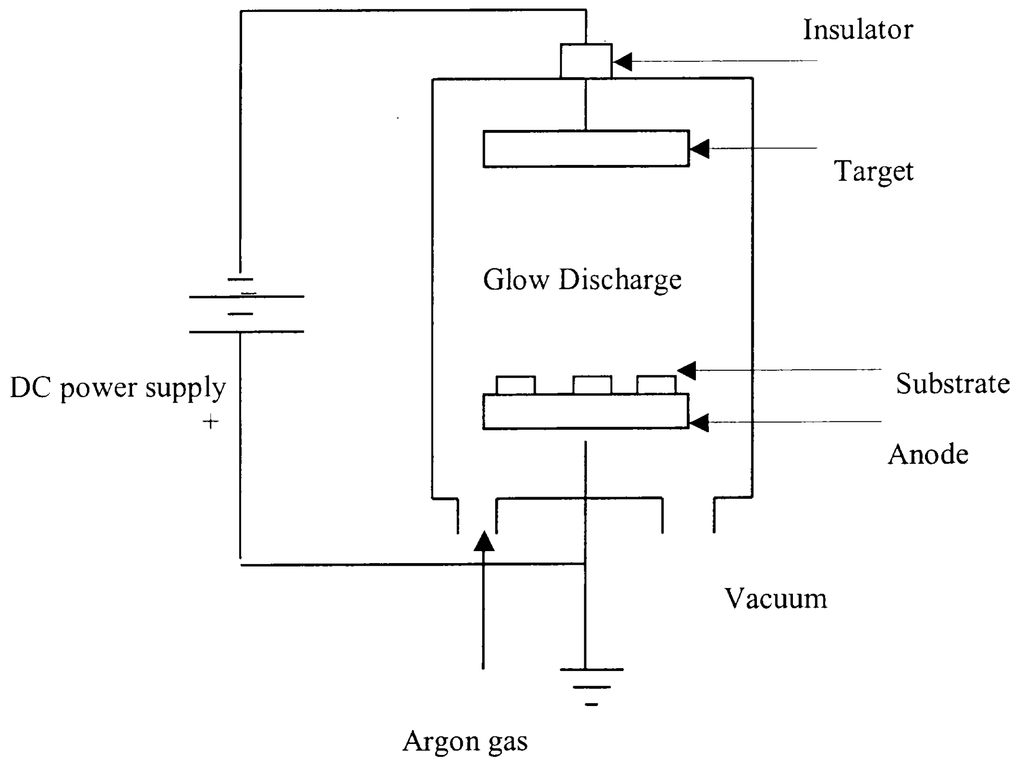

Fig 2.1 Schematic of a dc sputtering system

2.3 Magnetron Sputtering

The first sputter sources were designed as parallel plate diodes, which had no mechanism to confine electrons, emitted from the cathode. The resulting low sputter rates and substrate heating by electron bombardment were major problems. As the cross-section for electron impact ionization of the gas is fairly small, in dc diodes it is

usually necessary to operate at fairly high gas pressures (20-200 mtorr) to have a reasonable ion current. Such high gas pressures result in poor transport of the sputtered atoms away from the cathode and consequently result in very slow deposition rates. As a result dc diodes are rarely used in practical applications. Higher deposition rates can only be acheived by sources that operate at higher current densities, lower voltages and lower pressures than are possible in dc diode configurations.

The alternative sputter source that satisfies these requirements relies on a mechanism termed magnetron sputtering [15]. Converting the diode into a magnetron by adding magnets under the target, confines the electrons to spiral paths around the magnetic flux lines. The longer electron path length greatly increases the ionization probability and raises the plasma density. The maximum plasma density occurs where the magnetic flux lines are perpendicular to the electrical field lines. Current densities at the target are increased to 10-100 mA/cm^2, compared to about only 1 mA/ cm^2 for dc diode configurations. In addition, magnetron sources can sustain a glow discharge at much lower pressures than can dc diodes. A schematic of a typical magnetron source is shown in Figure 2.2 [16]. The auxiliary magnets help to distribute the magnetic field lines and increase the area where the magnetic field is perpendicular to the electric field.

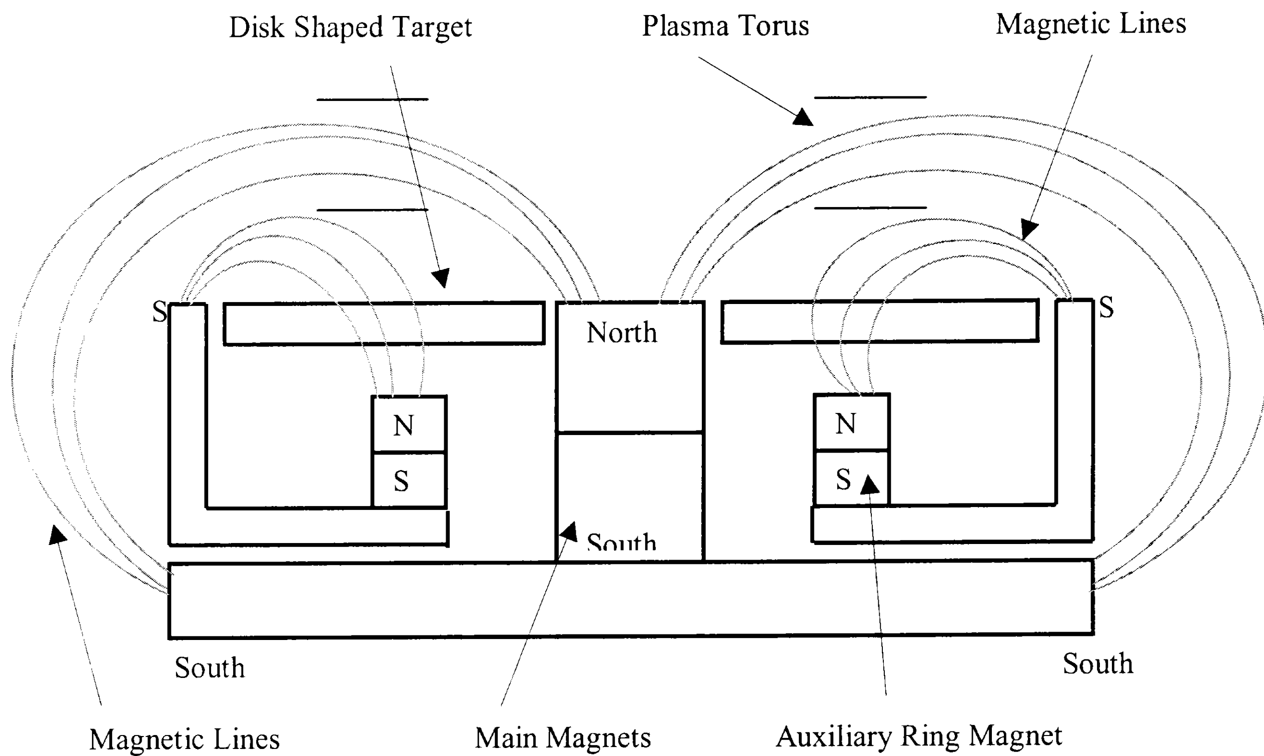

Fig.2.2 Schematic of a typical Magnetron Source [15]

2.4 Process Conditions That Affect Film characteristics

The important film characteristics [14, 15] influenced by the deposition process include

a) Correct thickness.

b) Thickness uniformity.

c) Low stresses in the deposited films.

d) Controllable grain sizes.

Events that occur as the sputtered atoms are transported in the reduced pressure gas phase between the target and the substrate have an impact on the deposited film characteristics. When the pressure in the chamber is high, the mean free path is short, and many collisions occur. A large fraction of the sputtered atoms thus gets scattered to the sidewall of the chamber or are redeposited onto the target surface. In the use of Argon, the sputtering gas, atoms whose masses are smaller than or are close to Ar suffer larger directional changes than those whose masses exceeds that of Ar. This is especially important when a binary alloy material is being sputtered, and the mass of atoms of one of the alloy materials is much smaller than the mass of the other which have a mass greater than that of Ar. The smaller atoms will get scattered more during vapor transport, and thus a smaller concentration of them will end up in the deposited film. Sputtering of tantalum with a heavy gas such as Kr (atomic mass 84 amu) increases the sputter yield and also, causes the impurities like oxygen or nitrogen to be scattered away.

Nearly all films are found to be in a state of internal stress, regardless of the means by which they have been produced. The stress may be compressive or tensile. Compressively stressed films would like to expand parallel to the substrate surface, and in the extreme, films in compressive stress will buckle up on the substrate. Films in tensile stress on the other hand would contract parallel to the substrate, and may crack if their elastic limits are exceeded. Highly stressed films are undesirable because they are more likely to exhibit poor adhesion and also, are more susceptible to corrosion. The total stress in a film is the sum of a) any external stress b) thermal stress and c) the intrinsic stress. Thermal stress results from the difference in the coefficients of thermal expansion between the film and the substrate. The thermal stress, σ_{th}, is due to the constraint imposed by the film-substrate bonding and for a given temperature difference ΔT is given by:

$$\sigma_{th} = (\alpha_f - \alpha_s)(\Delta T) E_f \tag{2.1}$$

Where α_f and α_s are the coefficient of thermal expansion for the film and substrate respectively, and E_f is the Young's modulus for the film. For tantalum film on steel, the thermal stress is compressive as the coefficient of thermal expansion for tantalum is smaller than that of steel. The intrinsic stress results from the structure of the growing films. It depends on method of film preparation, thickness, deposition rate, deposition temperature, process pressure and type of substrate used, among other parameters.

Thin films have generally smaller grain size than do bulk materials. Grain size is a function of the deposition conditions and post deposition annealing temperatures. Larger grains are observed in thicker films and raising the substrate temperature during deposition enhances this effect.

2.5 Literature Review

Researchers have varied different process parameters to obtain either the α or the β phase of Tantalum. However most of the conclusions differ. This may be because the formations of the phases are caused by the combined effect of different process parameters.

2.5.1 Film Purity

Read and Altman [8] observed the formation of β tantalum when the vacuum conditions are very clean with regard to reactive gases in the system. However Schauer et al [17] concluded based on their experiments that the formation of the β phase is an impurity stabilized phase with a certain relatively small amount of foreign atoms built into the tantalum film. They noted that clean substrates and clean conditions with regard to the reactive gases maintained during sputtering, produced the α phase.

2.5.2 Effect of Substrates

Feinstein and Huttemann [18] studied the effect of substrate on the formation of the tantalum phases. Tantalum was sputtered on twenty different substrate materials, which included single crystal, polycrystalline, and amorphous materials. The substrates were

classified based on their influence on the structure of tantalum that was formed. The substrates that were readily oxidized or formed surface oxides in air at room temperature (SiO_2, copper, nickel, amorphous glass) nucleated β tantalum. The substrates (Au, Rh, Pt and W) that do not form surface oxides even in oxidizing atmospheres always nucleated α tantalum. Finally the substrates which did not form surface oxides in air at room temperature but which can be oxidized at elevated temperatures always nucleated α tantalum when deposited directly on the substrate when the substrate was not oxidized. β Tantalum was formed when they were fully oxidized, while mixtures of both phases were formed when the substrates were partially oxidized. Shigehiko Sato [19] also, observed that substrates with a high resistance to oxidation tended to nucleate the bcc phase and substrates that readily formed oxides tended to yield β tantalum.

2.5.3 Effect of Underlayers

Westwood [13] researched the effect on tantalum films deposited on under layers of gold and gold on glass and polycrystalline alumina substrates. It was observed that the percentage of the bcc phase of tantalum was higher in films deposited on substrates covered by these underlays than in films deposited at the same time on adjacent substrates without underlays. Hoogeveen et. al. [20] observed that β tantalum always formed on SiO_2 and (111) textured copper, with the orientation of the Ta grains depending on the Ta layer thickness, whereas α Tantalum formed on a (111) aluminum underlayer. Sajovec et al [45] showed that α tantalum was always formed when deposited on an underlayer of niobium. This study also, revealed that minimum

thickness of 0.25 μ of niobium underlayer was required for the nucleation process of α tantalum. Tanaka et al [36] found that the phase of sputtered Ta formed on molybdenum underlayer depended on its thickness. As the thickness of molybdenum was increased, the percentage of the α phase formed was found to be higher. Hieber and Lautenbacher [32] found that β tantalum is also, stabilized by a tantalum silicide underlayer.

2.5.4 Effect Of Sputter Gas

Matson et al [55] studied the effect of using different sputtering gases. The gases used were Argon, Xenon and Krypton. The tantalum coatings produced using argon, as the sputtering gas were distinct from those produced using krypton and xenon. The krypton and xenon produced coatings were predominantly single phase α as indicated by XRD analysis. While the argon produced coatings were either β or α phase. The results suggests that the use of heavier gases promoted the formation of the bcc phase. Also, at high substrate temperatures in the range of 200 to 300 C, using krypton or xenon gas , bcc phase coatings were produced . Using argon as sputtering gas, substrate temperatures above 300 C are found to be necessary for formation of the bcc phase. The effects of sputter conditions on the crystal properties were investigated by Rottersman and Bill [21]. Tantalum films were deposited onto glass and Al_2O_3 with varying voltages in the range of 250 to 600 V. The films were deposited under argon-nitrogen mixtures. Films sputtered without nitrogen had the structure of β tantalum and the crystallographic properties and temperature coefficient of resistance were found to depend on the sputter voltage and/or argon pressure. A change in film structure from β

tantalum to α tantalum was observed at about 5 at. % nitrogen. No further change in crystalline structure occurred as the nitrogen content increased to 34 at. % with increasing flow rate. These results are consistent with that of Stavrev et al. [44]. Feinstein and Gerstenberg [28] studied the effect of varying oxygen content on the structural properties of tantalum while sputtering onto different substrates. Tantalum was deposited by dc diode sputtering at 6.6 kV and 300 mA onto Corning 7059 glass, quartz, sapphire and Ta_2O_5 coated Corning 7059 glass substrates using argon as the sputtering gas. The β tantalum phase is obtained for films containing no oxygen. Solubility of O_2 in the β phase is observed to be about 5 at. % after which a phase related to TaO_z appears. At 13 at. % O_2 bcc Ta diffraction lines are seen and grow in intensity with increasing O_2 content as the amounts of the first two phases decrease. Schauer and Roschy [22] used RF sputtered tantalum where the β phase was always formed with the addition of oxygen over the partial pressure in the range upto $1x10^{-4}$torr.

2.5.5 Substrate Bias

Another parameter, which has been reported to affect the tantalum structure, is the substrate bias. Phillippe Catania et. al. [23] reported that higher substrate bias (-100 V) induced the formation of the β phase. However different results have been obtained for different process conditions by other researchers. Matson et al [53] reported that higher substrate bias of –110 V caused the formation of the α phase. These findings are consistent with that reported by others, that higher substrate biases favor the formation of the α phase.

2.5.6 Substrate Temperature

Matson et al [9] observed that the substrate temperature influenced the film growth characteristics. At temperatures as low as 350 °C, mixtures of bcc and beta tantalum were formed. In their study, AISI 4340 steel substrates were heated by thermionic emission over a period of 30 minutes by applying a potential of 60 V between the heated tantalum filament and the anode. Upon completion of the substrate heating, the substrate was etched by ion bombardment, following which sputtering was carried out. At substrate temperatures of 450 °C, 72 % of the deposited tantalum had bcc structure. This study was carried out using krypton as the sputter gas. Lee et al also, studied the effect of substrate temperature on the tantalum phase formation using krypton as the sputter gas on AISI 4340 steel substrates. Heating of the substrates was done by the same technique used by Matson et al [9]. The results indicated that elevated substrate temperatures in the range of 200 to 300 °C were conducive to the formation of a complete tantalum α phase coating. These experiments were carried out in a cylindrical geometry triode sputtering system. They concluded that the combination of improved gas purity resulting from system preheating and the use of a catcher rod to improve oxide and metallic impurities from initial tantalum deposits allowed them to produce single-phase bcc tantalum deposits at substrate temperatures in the range of 200 to 300 °C. Fischer et al [27] deposited Ta films at substrate temperatures of 400 °C. It was found that at substrate temperatures below 400 °C the beta phase was formed while above this temperature bcc phase of tantalum was formed. These experiments were carried out using argon as the sputter gas on silicon substrates. No details of the heating process are mentioned. Schwartz et al [39] demonstrated that mixtures of α and β phases could be deposited by sputtering at

substrate surface temperatures of 400- 465 °C. The Corning glass 7059 substrates were heated during sputtering by heaters to temperatures in the range of 270 to 480 °C and thin film thermocouples were calibrated to read the surface temperature of the substrates during sputtering. Mattox et al [62] observed the formation of mixture of α and β phases on substrates heated to a temperature range of 300 – 600 °C. Graphite and tantalum substrates were heated during deposition for this study.

Schauer et al [22] deposited tantalum films on Corning 7059 glass and Ta_2O_5-coated substrates at a temperature above 300 °C. The substrates were preheated in the chamber following which sputtering was done. It was seen that most of the films deposited onto the substrates at a temperature higher than 300 °C produced pure α phase while a few of the films showed mixtures of α and β phases. Heiber et al [32] used Corning 7059 glass and sapphire as substrates for tantalum deposition. The substrates were heated to temperatures above 300 °C during sputtering. Mixtures of α and β phases were formed. Mills [11] heated 7059 glass and polished quartz to temperatures ranging from 300 to above 600 °C. A tungsten heater filament heater was used for preheating of the substrates. Above 600 °C the structure of the coatings was observed to be pure α phase, while the coatings deposited on substrates at temperatures in the range of 300-600 °C showed mixtures of α and β phases.

CHAPTER 3

CHARACTERIZATION TECHNIQUES

3.1 X-ray Diffraction

3.1.1 Introduction

This technique uses the principles of diffraction to determine lattice constants and geometry, identification of unknown materials, orientation of single crystals, preferred orientation of polycrystals, defects, stresses etc [48,49]. The samples can be in the form of powder, solids or thin films. The X-ray pattern of the crystalline substance can be thought of as a 'fingerprint', each crystalline material having, within limits, a unique diffraction pattern

3.1.2 Description

If a beam of monochromatic X-rays is directed at a crystalline material, diffraction of the X-rays are observed at various angles with respect to the primary beam. The relationship between the wavelength of the X-ray beam, λ, the angle of diffraction, 2θ and the distance between each set of atomic planes of the crystal lattice, d, is given by Bragg's law as:

$$n\lambda = 2d \sin \theta \qquad (3.1)$$

where 'n' represents the order of diffraction. From this equation, the interplanar distances of the crystalline material can be calculated. The interplanar distances depend solely on the dimension of the crystal's unit cell, whereas the intensities of the diffracted rays are a

identified by comparing the interplanar spacings and intensities of its pattern to the patterns in the powder diffraction file of the International Center for Diffraction Data (ICDD). The schematic of the XRD setup is shown in Figure 3.1.

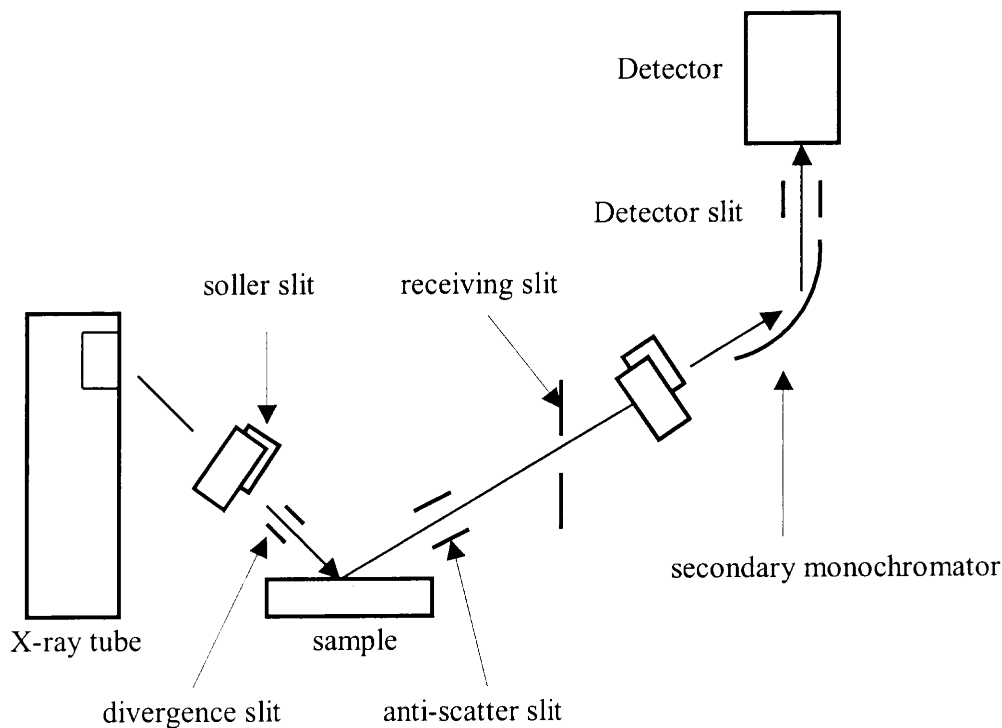

Fig. 3.1 Schematic of XRD setup.

An important factor to be considered during x-ray diffraction is the structure factor for different crystal structures. Each atom in the unit cell will scatter an x-ray beam of intensity given by the atomic scattering factor f and with a phase depending on its location in the cell. The resultant scattering from all of the atoms in the unit cell for a

diffraction line is called the structure factor F_{hkl}. The intensity that is observed for any Bragg reflection is proportional to $| F_{hkl}^2 |$. Therefore from the position of the atoms in the unit cell (x, y, z) the structure factor can be calculated and related to the intensity.

The orbing depth of the x-ray beam into the sample depends on the x-ray absorption length for the material at the beam energy. XRD has advantages because it is non-destructive and does not require elaborate sample preparation or film removal from the substrate.

3.2 Scanning Electron Microscopy (SEM)

3.2.1 Introduction

The SEM provides information related to topographical features, morphology, phase distribution, compositional differences, crystal orientation and the presence and location of electrical defects [48,49]. SEM is central to micro structural analysis and therefore important to any investigation relating to the processing, properties and behavior of materials that involves their microstructure .

The SEM is also, capable of determining elemental composition of micro – volumes with the addition of an x-ray spectrometer. The strength of the SEM lies in its inherent versatility due to the multiple signals generated, simple image formation process, wide magnification range, and excellent depth of field.

3.2.2 Description

Electrons thermionically emitted from a tungsten or LaB_6 cathode filament are drawn to an anode, focused by two successive condenser and objective lenses into a beam with a very fine spot size (~ 50 A°). Pairs of scanning coils located at the objective lens

deflect the beam either linearly or in raster fashion over a rectangular area of the specimen surface. Electron beams having energies ranging from a few thousand to 50 keV; 20 keV is a common energy are utilized. Upon impinging on the specimen, the primary electrons decelerate and in losing energy transfer it inelastically to other atomic electrons and to the lattice.

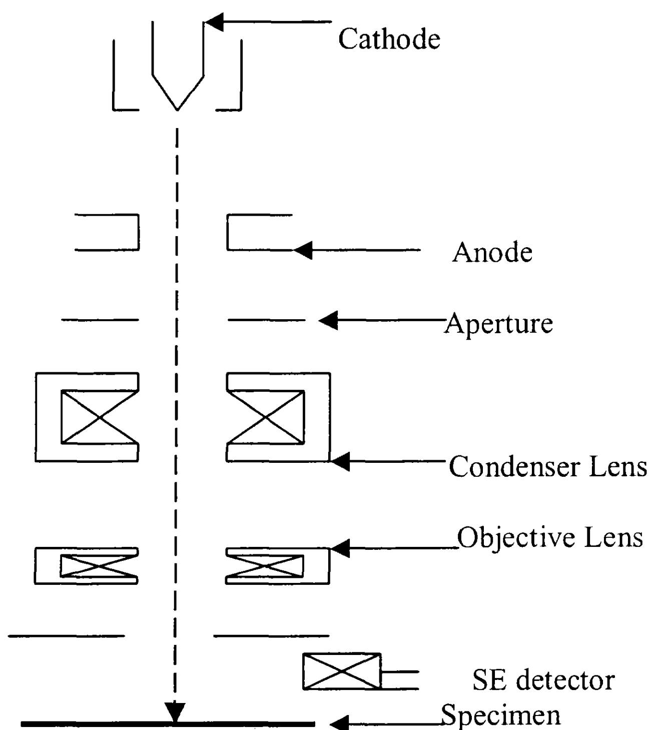

Fig 3.2 Schematic of SEM setup

Through continuous random scattering events, the primary beam effectively spreads and fills a teardrop-shaped interaction volume with a multitude of electronic excitations. The signals resulting from these interactions (electrons and photons) will each have different depths within the sample. Secondary electrons that have low energies (2 – 5 ev) are ejected from the outer shell of a sample atom after an inelastic

interaction. These low energy electrons can escape the surface only if it is generated near the surface. Backscattered electrons are electrons from the incident beam that undergo elastic interactions with the sample, change trajectory, and escape the sample. These make up the majority of electrons emitted from the specimen, and their average energy is much higher than that of the secondary electrons. The schematic of the SEM setup is shown in Figure 3.2.

The SEM image conveys three – dimensional information due to the depth of field in the image. The depth of field depends on the electron beam divergence angle, which is defined by the diameter of the objective lens aperture and the distance between the specimen and the aperture. This angle is exceptionally small compared to that in an optical microscope and results in a small change in diameter of the beam with change in distance from the lens. This means that the sampling volume can likewise remain small over this range of depth. All points will appear in focus where the sampling volume diameter is smaller than the picture element. Depth of field is increased by reducing the beam divergence angle, which can be done by increasing the working distance or decreasing the aperture diameter. The resolving power of the SEM is dependent upon the sampling volume, since this sampling volume is the portion of the specimen from which the signal originates.

In SEM only conducting samples can be used. If an insulating specimen is used then the absorbed electrons accumulate on the surface since no conducting path to ground exists. The accumulation of electrons builds up a charge region. This can actually deflect the beam in an irregular manner, leading to severe image distortion. Environmental SEM (ESEM) is used for liquid and hydrated samples. To balance the

effect of negative charge buildup on a sample surface, sufficient positive charged ions are required. They are supplied by an ionizing gas typically water in the sample chamber.

3.3 Energy Dispersive X-ray Spectroscopy

3.3.1 Introduction

EDX is used to determine elemental composition and quantitative information of the local composition of the material [48,49]. Most energy-dispersive X-ray analysis systems are interfaced to SEMs, where the electron beam serves to excite characteristic X-rays from the area of the specimen being probed.

3.3.2 Description

When an electron beam having energies typically 20 keV impinges on the surface of the specimen, it causing X-rays to be emitted from the specimen. The energy of the X-rays is specific to the elements present in the specimen. EDX detector is normally attached to the SEM column, in the form of a liquid –nitrogen cooled Si (Li) detector aimed to efficiently intercept emitted X-rays. The Si (Li) detector is a reverse biased Si diode doped with Li to create a wide depletion region. An incoming X-ray generates a photoelectron that eventually dissipates its energy by creating electron-hole pairs. The incident photon energy is linearly proportional to the number of pairs produced, which is proportional to the amplitude of the voltage pulse generated in the detector circuit. The pulses are amplified and then sorted according t voltage amplitude by a multi channel analyzer, which also, counts and stores the number of pulses within given increments of the energy range. The result is a characteristic X-ray spectrum for the elements. Si (Li)

detectors typically have a resolution of about 150 eV, so overlap of peaks occur when they are not separated in energy by more than this amount. Elements of lower atomic number are difficult to detect. This is because a Beryllium window often protects the SiLi detector. The soft X-rays are absorbed by Be which precludes detection of elements below sodium (atomic number 11). The X-rays are generated in a region of about 2 μm in depth but electron beam and thus EDX is a surface analysis technique.

3.4 X-ray Fluorescence Spectroscopy (XRF)

3.4.1 Introduction

XRF is used for qualitative and quantitative analysis of elemental composition in a wide range of materials [48,49]. For XRF to be effective, the specimen must be subjected to high intensity X-rays, very sensitive detectors and suitable optics.

3.4.2 Description

When an atom,is irradiated with highly energetic photons an electron from one of the inner shells is ejected in the form of a photoelectron. As an electron from an outer shell fills the vacant place, a photon whose energy is characteristic of the atom is released. This radiation is called the fluorescent radiation, and each element has its own set of characteristic emission or XRF lines. Also, the intensity of emission- number of photons – is proportional to the concentration of the specific element in the sample. The intensity and the energy of these lines are measured using a spectrometer. In the wavelengths of dispersive X-ray fluorescence spectrometer, a crystal grating is used to separate the energies and a conventional X-ray detector measures the intensities. The principles of spectrometer is based on Bragg's law of diffraction, equation (1).The analyzing crystal

with lattice planes parallel to its surface and separated by distance d is used to separate the various wavelengths by diffraction. By changing the angle θ, by rotating the crystal, different wavelengths are diffracted. Single crystals such as Ge or Lithium fluoride are normally used. A rotating optical assembly called the goniometer enables any number of elements to be measured. This involves moving the analyzing crystal through increments of θ while a detector rotates through 2θ to intercept the diffracted beam. Use of computer softwares has enabled semi quantitative analysis without the use of internal standards. The software calculates the XRF spectrum for a given radiation using a certain number of standards, which cover nearly every element in the periodic table. The program calculates the composition by a least squares fit of this predicted spectrum from the standards to the observed intensities from the unknown specimens.

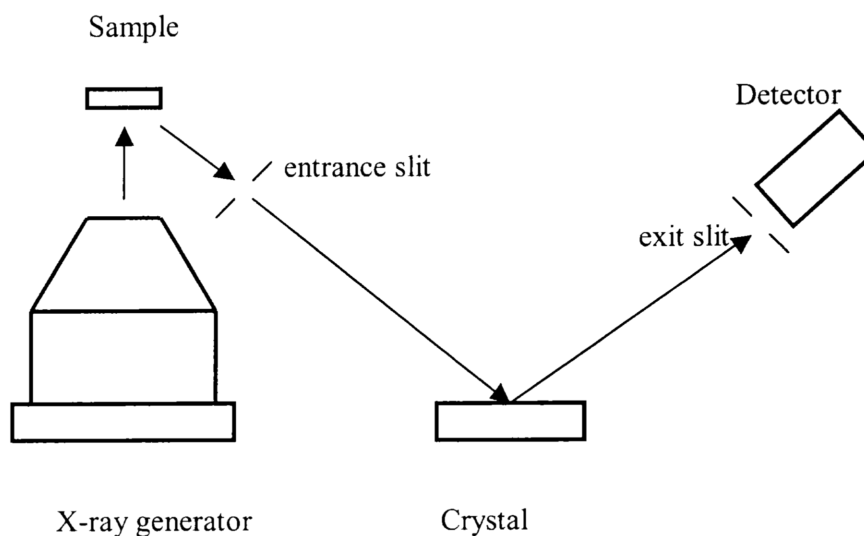

Fig 3.3 Schematic of XRF setup.

The primary limitation of XRF is the decrease in the sensitivity for elements lighter than aluminum. This is due to absorption of low energy X-rays in the specimen itself. Also, for accurate quantitative analysis, standards that are similar in composition and morphology to the unknown are usually required.

3.5 X-ray Absorption Fine Structure Spectroscopy (XAFS)

3.5.1 Introduction

X-ray absorption fine structure spectroscopy is a final state interference effect involving scattering of the outgoing photoelectron from the neighboring atoms [33,34]. XAFS is a technique to determine the local structure around specific atomic species in solids, liquids and molecular gases. In this technique the X-ray absorption coefficient μ is measured as a function of photon energy above the threshold of an absorption edge. Among its strengths are its usability to amorphous materials and its ability to probe the local structure around each species in the sample by selecting the incident x-ray energy.

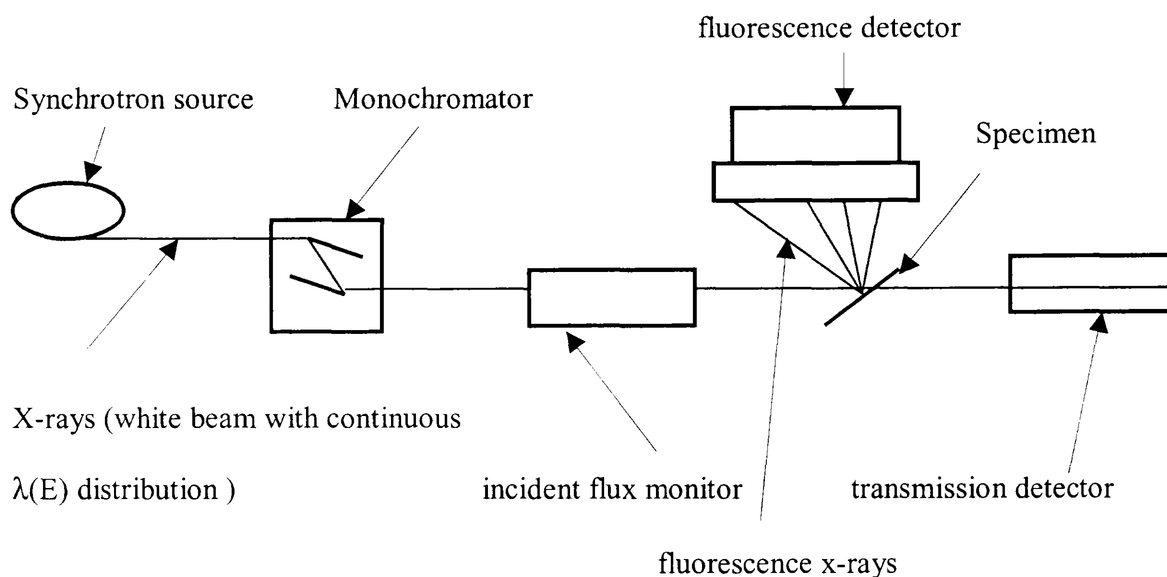

Fig. 3.4 Schematic of XAFS experiment

3.5.2 Description

Polychromatic X-rays are produced by a synchrotron radiation source and a desired energy band of approximately 1 eV bandwidth is then selected by diffraction from a silicon double crystal monochromator. Only those x-ray photons that are of the correct wavelength λ to satisfy the Bragg condition $n\lambda = 2d \sin\theta$ at the selected angle θ will be reflected from the first crystal, the others are absorbed. The parallel second crystal is used as a mirror to restore the beam to its original direction. The monochromatic x-rays are then allowed to pass through the sample which absorbs approximately 50 – 90% of the incident x-rays. The incident and transmitted or the fluorescence fluxes are monitored usually with gas ionization chambers.

The linear absorption coefficient μ, consists of two components. The first is μ_0, the absorption of an atom in the absence of any neighbors. The other is χ which is dimensionless and depends on the oscillatory component of μ, arising from self-interference of the photoelectron reflected back onto it by neighboring atoms. χ is therefore a ratio and is given by

$$\chi(k) = \frac{\mu - \mu_0}{\mu} \qquad (3.2)$$

The amplitude of the back-reflected wave will be related to the repulsive field of the neighboring atoms and the number of neighboring atoms in each successive shell away from the central atom. The amount of interference will further depend on the phase of the back reflected wave, which in turn depends on the distance of the scattering neighbor atom from the central atom being ionized, and the wavelength of the photoelectron. The EXAFS equation is thus given as

$$\chi(\kappa) = - \Sigma \{ [N_i / (k r_i^2)] F_i(k) S_0^2(k) . \exp[- r_i / \lambda_d(k)] . \exp(-2 k^2 \sigma_i^2)$$

$$\sin(2k r_i + \phi_i) \} \qquad (3.3)$$

which applies to the photoexcitation of a 1s electron (K edge) in a polycrystalline sample. This equation expresses the EXAFS function as a sum of contributions, one for each shell of neighboring atoms. Each atomic shell contains N_i atoms of type *i* at a radial distance r_i from the absorbing atom. A shell centered at r_i contributes with a sinusoidal function of wavelength $\cong \pi / r_i$ in k space. The phase of each sinusoidal function is related to the distance r_i of the neighboring atoms from the central atom, and to the phase shift ϕ_i introduced by the potentials of central and backscattering atoms. The envelope of each sinusoidal function is determined by the number of atoms in the shell and by the amplitude of the backscattering factor F_i. The damping terms in the equation take into account multibody affects, S_0^2, inelastic scattering, $\exp(- r_i / \lambda_d)$, and thermal and structural disorder, $\exp(-2 k^2 \sigma_i^2)$. Fourier transforms of the background corrected EXAFS signal, produces the atomic radial distribution for the absorbing central atom in the material.

The strong oscillations, which extend beyond the edge for about 30 – 40 eV are called the X-ray absorption near-edge structure (XANES). This involves the multiple scattering of the excited photoelectrons and is determined by the geometrical arrangement of atoms in a local cluster around the absorbing atom. XANES yields information regarding the nature of unoccupied electronic states of the atom in question.

The precise position of the absorption edge can give the iconicity of the central atom. EXAFS suffers from the lack of low momentum data. Therefore, in moderately disordered systems, information on second and higher order shells may be absent. The main shortcoming of XANES is the lack of a readily applicable quantitative theory to correlate the data and the structural model.

3.6 Transmission Electron Microscopy (TEM)

3.6.1 Introduction

Transmission electron microscopy can be used to study the local structure, morphology, and chemistry of materials by examining the diffracted and transmitted electron intensities as well as the characteristic X-rays and the energies lost by the incident beam. Transmission electron microscopes are either of the scanning type called STEMs if the incident beam is rastered or of the conventional type TEM if the beam is stationary. TEMs are also, often interfaced with EDX to obtain information of local chemistry of the material.

3.6.2 Description

A beam of high energy electrons, typically 100-400 keV is generated in the gun chamber [63].The electron source can be a tungsten filament, a LaB_6 crystal, or a field emission gun. The generated beam is then collimated by magnetic lenses and allowed to pass through the specimen under high vacuum. The condenser lens focuses the electrons to a small thin coherent pinpoint beam. The aperture restricts the beam by knocking out high angle electrons. The diffraction pattern resulting from the passage of the beam through

the sample consists of a transmitted beam and a number of diffracted beams, which can be imaged on a fluorescent screen below the specimen. From this diffraction pattern the lattice spacing and symmetry information of the observed specimen can be obtained. Also, the transmitted beam or one of the diffracted beams can be used to form magnified image, of the sample on the viewing screen. These are, respectively, the bright and dark-field imaging modes, which give information about the size and shape of the microstructural constituents of the material. Also, if the transmitted beam and one or more diffracted beams are allowed to recombine, a high resolution image that contains information about the atomic structure of the material can be obtained.

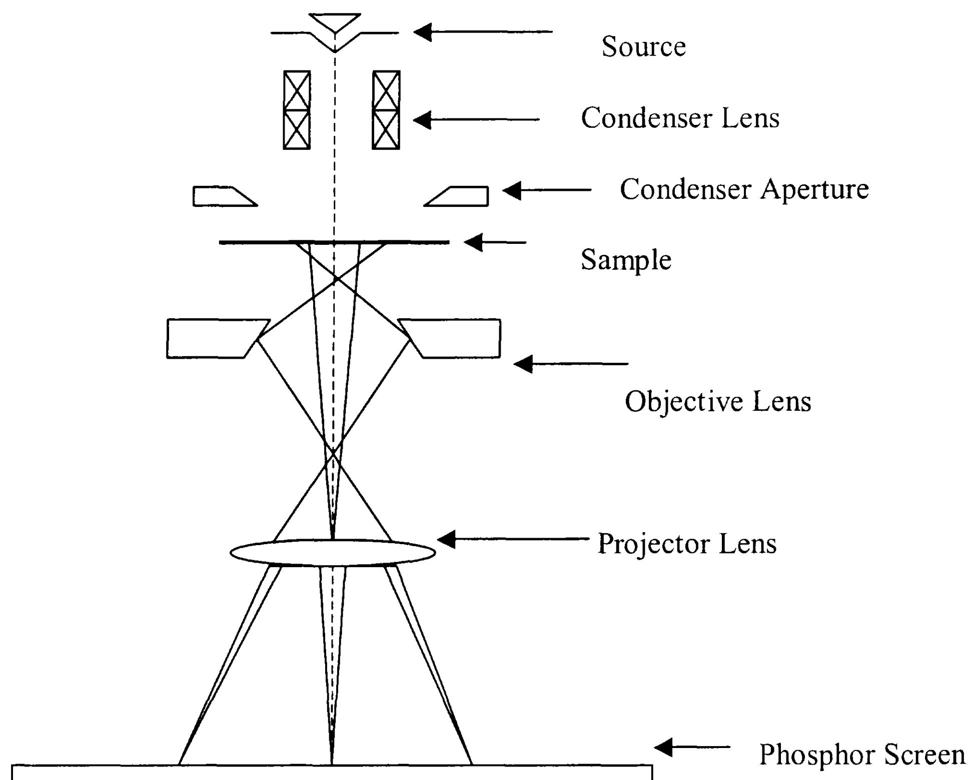

Fig. 3.5 Schematic of TEM set up.

Most solid materials can be studied, but because of the large scattering of the electrons in the solids, samples are limited to no more than 3 mm in diameter and less than 100 Å in thickness. In the area of interest, however the sample has to be thin, typically less than 0.2 μm enough to be transparent to the electron beam. A critical aspect of TEM involves obtaining a thin enough sample. Various techniques have been developed for this, which include spraying or dusting, electropolishing, ion milling and tripod polishing.

The drawback of TEM is sample preparation, which is time consuming and complicated. Also, some materials, especially polymers are relatively sensitive to electron beam irradiation, resulting in loss of cystallinity and/or mass. The TEM is such constructed that either the image of the diffraction pattern or the image of the detail in the specimen can be viewed on the fluorescent screen of the instrument. Alternatively, both of these images can be photographed on a plate or film. This is possible because of a projection lens system located in the microscope. This lens system can be adjusted to project either the image of the diffraction pattern or that of the specimen onto the fluorescent screen. The diffraction pattern from a set of planes is in the form of rings. A spot pattern is obtained when the specimen is tilted in its stage so that an important zone axis is placed parallel to the microscope axis. The spots corresponds to the planes of the zone whose axis parallels the electron beam.

3.6.2.1 Sample Preparation The specimen is prepared for TEM by first cutting it into 3 mm discs, which are later thinned and polished using dimplers and ion mills [63]. The sample is cut using an adjustable- sped drill press that is equipped with a soft metal core and a diamond impregnated drill to produce the required cut specimens. This process is

followed by ‘tripod polishing’ in which the ‘tripod’ holder sets the sample height and angle with micrometers to guarantee precise control of the lapping position. Diamond lapping films and precisely flat glass lapping surfaces are used to ensure a smooth finish on cross-sectioned and plan view samples. This is followed by prethinning with a dimpler, prior to ion milling to reduce the sample preparation time by ion milling. Prethinning with the dimpler reduces the sample preparation time in an ion mill from 20 – 25 hours to as little as five minutes. The dimpler uses a grinding wheel, which rotates about a horizontal axis and rests on a specimen platform , which rotates about a vertical axis. During grinding the wheel is gently lowered onto the specimen and a sensitive dial indicator shows the specimen thickness. Grinding is halted when a preset thickness (down to 5 –10 microns) is reached.

Ion milling is used as the final step for preparing high quality TEM specimens. The ion milling system has either two or three ion guns each with an input power of approximately 2 W at 5 kV accelerating voltage. These guns are fixed on fully adjustable flanges so that they can be aligned to the upper and lower side of the sample. The sample is fixed on a holder inside the stage, which can be rotated, rocked and tilted. The tilting angle can be varied between 0 and 30 °. The impinging ion beam etches away material from the surface of the specimen thus thinning it. The possibility of etching at very small angles of less than 5 ° reduces thermal stresses on the specimen. To provide widely transparent areas it is necessary to stop the etching process immediately when the first hole occurs, otherwise the thinned area would be destroyed. In order to monitor the generation of holes in the sample, a weak ion beam (approx. 0.9 kV) is produced by a small ion gun, which is fixed perpendicular to the sample; an ion detector detects the

holes down to 20 μm. In spite of its universal applicability this method has its drawbacks such as significantly damaged specimen surface that makes their high-resolution study difficult or even impossible. It is relatively a slow way of material removal and the small but finite material selectivity of the ion thinning rate results in poor quality pictures in the case of specimens made of components of very different atomic number.

CHAPTER 4

TANTALUM DEPOSITION

4.1 Introduction

Samples used for this study were either deposited at Bennet Laboratory [64] or at the Ion Beam and Sputter Lab, NJIT [65]. The details of the samples are tabulated in Table 4.1 below. The deposition process done at NJIT is described below. Even though most details of the samples deposited at Bennet Labs are not known, the Description below is representative for all the deposited samples.

4.2 Deposition Process

The planar sputtering system consists of a stainless steel cylindrical sputtering chamber, 15 inch long and 20 inch in diameter. It is designed to hold 8 substrate holders, each of which can hold 6 substrates of dimensions 12.5 x 12.5 cm and thickness of 5 mm. The sputtering source is Tourus 2-inch make supplied by Kurt Lesker and has permanent magnets fitted inside it, which helps in confining the electrons nearer, the target surface. The 2-inch diameter, tantalum target, 1.125 inches thick with a specified purity of 99.95 % is cooled by water circulation. The substrates are positioned circularly on a revolving platter, which are brought successively over an open window in a fixed stainless shield in the line of sight of the target. The target to substrate distance is maintained at 4.5 inches.

Table 4.1, Details of samples used in this study

Sample Name	Approx. thickness in Angstroms, Å	Substrate	Deposition rate, Å/ min	Sputter Gas	Other conditions	Prepared at
A and B*	25000	AISI 4340 steel	Not known	Argon	Planar magnetron sputtering system	Bennet Laboratory
C	5000	Silicon	500	Argon	Unheated	NJIT
D	5000	Silicon	500	Argon	Preheated to 321 °C	NJIT
E	5000	AISI 4340 steel	500	Argon	Unheated	NJIT
F	5000	AISI 4340 steel	500	Argon	Preheated to 321 °C	NJIT
G	2000	Silicon	660	Argon	Unheated	NJIT

* For these two samples the target was held 2 inches above the steel substrate during deposition. The sputtering gas was Argon at 10 mTorr. The estimated substrate temperature was <100° C.

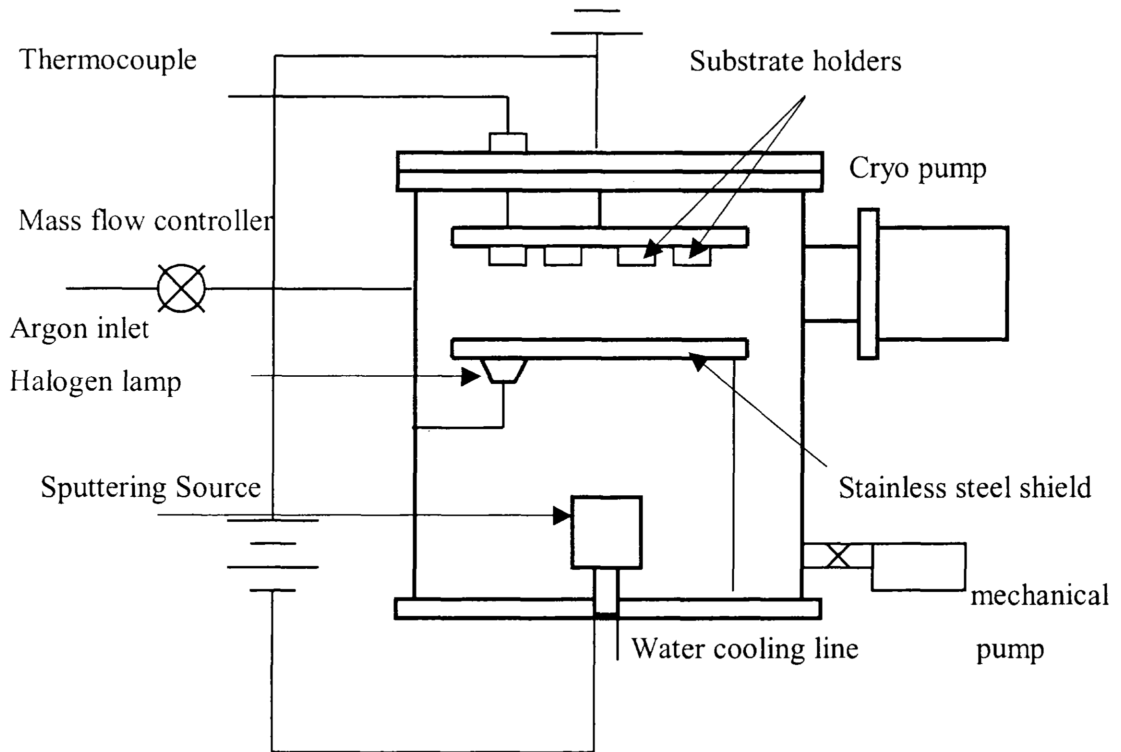

Fig. 4.1 Schematic of the sputtering system

The chamber was pumped down to vacuum by a mechanical pump, model no. D8B, Leybold make to a pressure of 100 mtorr. Further pump down to lower pressures of 1 x 10 $^{-7}$ torr was done by a cryo pump, model no. Cryopump 8 made by CTI Cryogenics. Argon of 99.999 purity was used as the sputter gas; a mass flow controller controlled the flow to the sputtering chamber. The chamber was prebaked to a temperature of 250 °C for a period of 5 hours. After baking, the chamber was cooled and pumped down to a

base pressure of 1 x 10 $^{-7}$ torr for a duration of 12 hours. Gun steel and silicon substrates were used for this experiment. The steel substrates were ultrasonically cleaned in four steps. First, in a detergent solution of Alconax, then in propanol followed by cleaning in acetone and lastly again in propanol. The silicon substrates were ultrasonically cleaned in propanol followed by acetone and then again with propanol. The silicon substrates were not cleaned using Alconax, a detergent as residues of it may remain as moisture on its surfaces and thus effect the quality of the sputtered films. Preheating of the steel and silicon substrates, samples D and F was done just before sputtering using a halogen lamp of 200 W till thermal equilibrium was reached at 321 °C. The temperature of heating was controlled by varying the power of the lamp using a variac. Sputtering was done immediately after heating for 10 minutes at a voltage of 330 volts and current of 2.8 amperes at a pressure of 12.9 mtorr. The flow rate of argon was controlled to 12 sccm. Sample G used for TEM analysis was sputtered for approximately 3 minutes. This was done for ease in TEM sample preparation.

4.2.1 TEM Sample Preparation

Sample preparation was carried out by RG Lee Group, PA [57]. A portion of the sample was first cleaved to create a specimen of approximately 3mm square. A Southbay make tripod polisher equipped with a Pyrex insert was used to hold the sample for further mechanical thinning. Copper grid with a 1mm x 2 mm opening was attached to the film surface with an adhesive, which was used to further attach the sample to the Pyrex insert. Silicon from the substrate was removed by grinding and polishing using the following sequence of media: 600 grit Silicon carbide (SiC), 1200 grit SiC, 3 μ diamond, 0.3 μ

diamond and 0.1 μ diamond. The specimen was polished to a low angle wedge using 0.1 μ diamond grit polish thereby providing electron transparency at the thin edge of the specimen. At the end of polishing, the specimen was rinsed with four consecutive applications of acetone to remove the adhesive and dried and placed into a bean capsule for storage before TEM inspection. A JEOL 2000 FX instrument at 120 kV was used for the TEM analysis. TEM images and electron diffraction patterns were collected from the specimen. The images showed the texture of the tantalum film, while the diffraction pattern consisted of concentric rings of which the d-spacings were measured. The results showed only α Tantalum diffraction rings. XRD done after this initial analysis revealed diffraction peaks, which matched that of β Tantalum. The TEM analysis was then repeated for another specimen prepared from the same sample to detect any β Tantalum diffraction patterns. The specimens were found to be cracking during the TEM analysis work. Therefore, the specimens could not be reused for further testing.

CHAPTER 5

ANALYSIS OF SAMPLES

5.1 Introduction

The results of the characterization study of all the samples are described below. The characterization techniques used for the samples are tabulated in Table 5.1 below.

Table 5.1, Details of characterization techniques used. Y= Yes, N= No

Sample name	XRD	XRF	EDX	SEM	XAFS	TEM
A and B	Y	Y	Y	Y	Y	N
C, D, E and F	Y	Y	N	N	N	N
G	Y	Y	N	N	N	Y

5.2 X-ray Diffraction Analysis

The X-ray diffraction was performed using a Philips X-ray diffractometer of model X'Pert-MPD XRD system, Serial No. D4715 with PC-APD software. Operating parameters of 40mA and 45 kV were used to generate Cu K-α x-rays. Data were collected over a 2θ range from 10° to 110° for a period of 24 hours for samples A and B. The samples C, D, E, F and G after deposition of Tantalum were characterized by XRD

indexed by the standard powder diffraction pattern data for bcc tantalum, from JCPDS ref. Card no. 04-788 and β tantalum, JCPDS ref. Card no. 25-1280 [40]. The diffraction results reported by Read et al [8] for β tantalum coatings were also, used for confirming the observed patterns.

The diffraction peaks of sample A, Figure 5.2 are similar to the corresponding peaks of Tantalum powder, Figure 5.1 and also, match the JCPDS data file for bcc tantalum. This shows that the α phase has the same structure as Tantalum powder, which is bcc. The diffraction peaks of sample B, Figure 5.3 was originally indexed as β (002), β (513) and α (321). However this can be indexed as β (002), β (004) and β (006) [58]. The d-spacings for these indices are 2.67 Å, 1.32 Å and 0.67 Å respectively. These indices are of a single crystal β Tantalum.

All the samples have β (002) diffraction peak. Tantalum film on heated Silicon substrate, sample D has α and β phases in the ratio of 40:60, Figure 5.4. The unheated Tantalum film on both the substrates, samples C and E, Figure 5.5 shows almost 100 % β phase. These results show a mixture of α and β Tantalum phases in the ratio of 25:75 formed on the preheated Steel substrate, sample F. The ratio of β: α phases in sample G was calculated to be 90:10. In the XRD results of the preheated Silicon sample D, ratio of the intensity of β (002) peak to α (110) is only ~1.3, while in all the other samples characterized by XRD the intensity of β (002) peak is observed to be higher at least by a factor of 7.

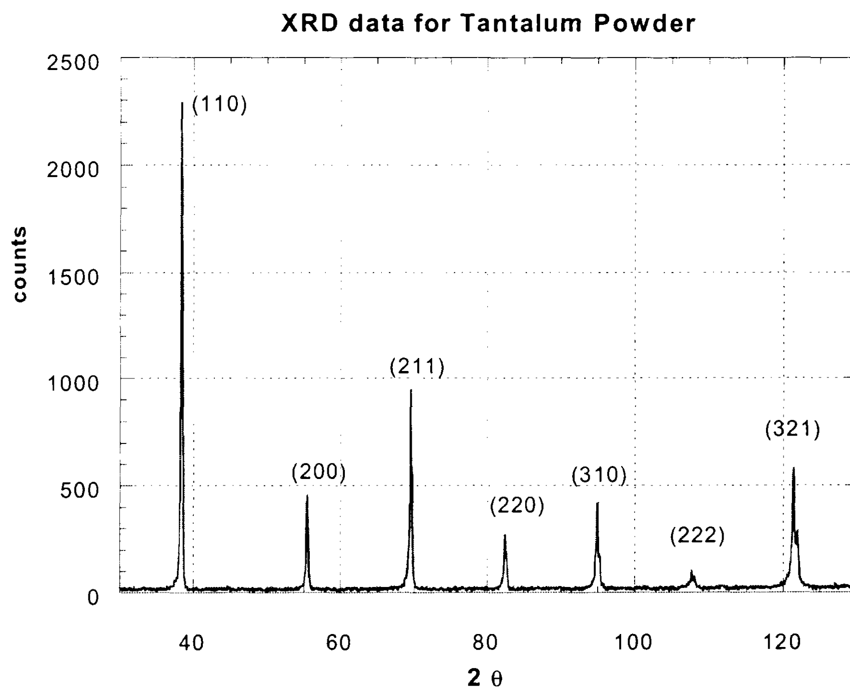

Fig. 5.1 X-ray scan for Ta powder

The diffraction peaks correspond to the standard powder diffraction pattern of bcc tantalum (JCPDS ref. card 04-0788). The relative intensities in this scan are in accordance with those of standard bcc phase.

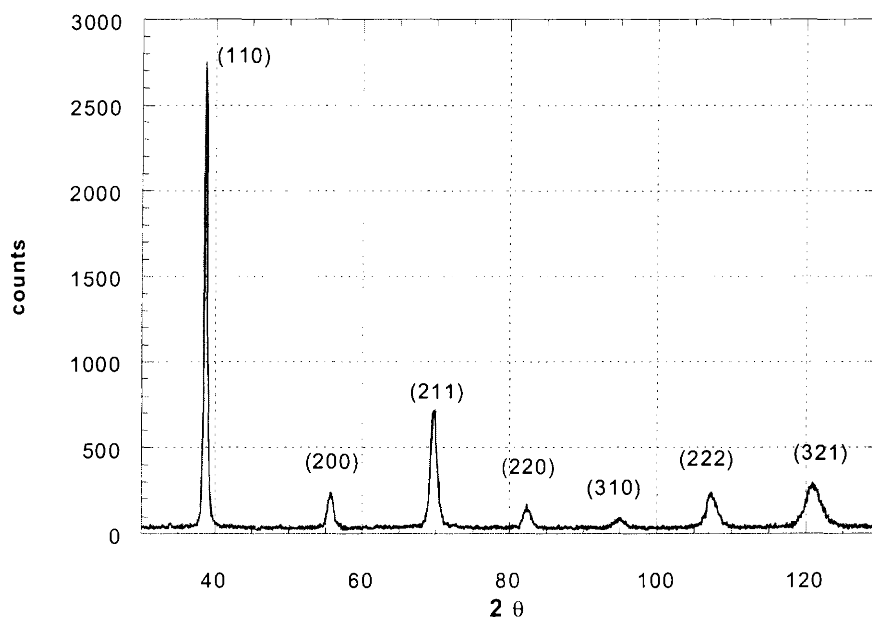

Fig. 5.2 X-ray scan for Ta film on steel substrate, Sample A

The diffraction peaks observed in this spectrum correspond to the peaks observed for Tantalum powder shown in the previous figure. Also, the relative intensities of the peaks are similar to those of Tantalum powder.

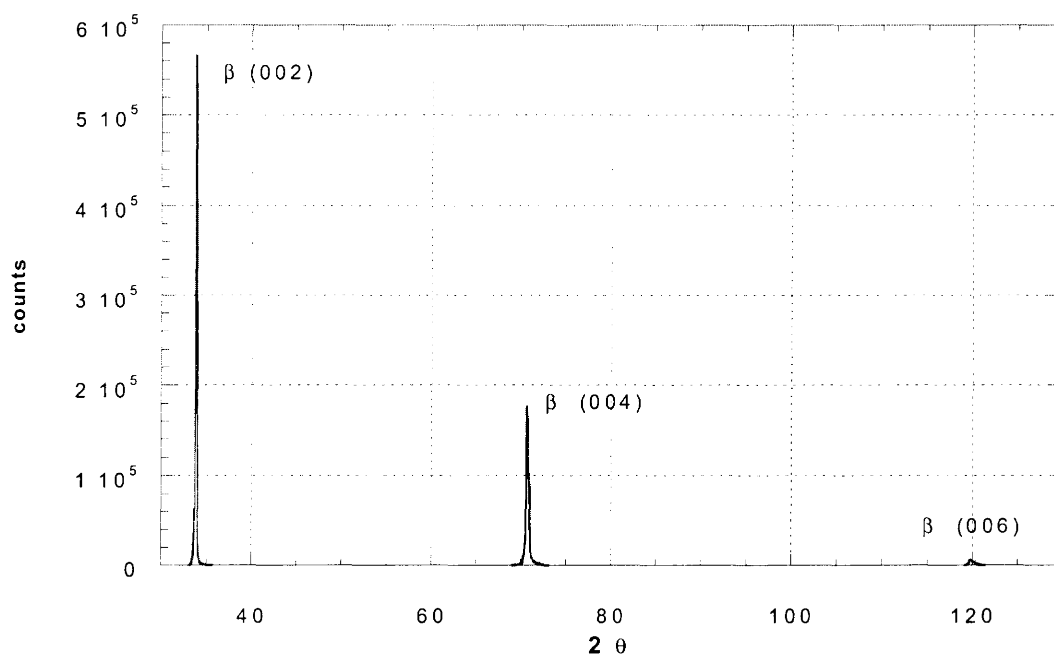

Fig. 5.3 X-ray scan for Tantalum film on steel substrate, Sample B.

The diffraction peaks correspond to the β phase of tantalum. The peaks were indexed as per the standard diffraction pattern for this phase (JCPDS ref. card 25-1280). The intensities of the peaks are seen to be higher than that of the Ta powder or the α phase peaks shown in the previous figures.

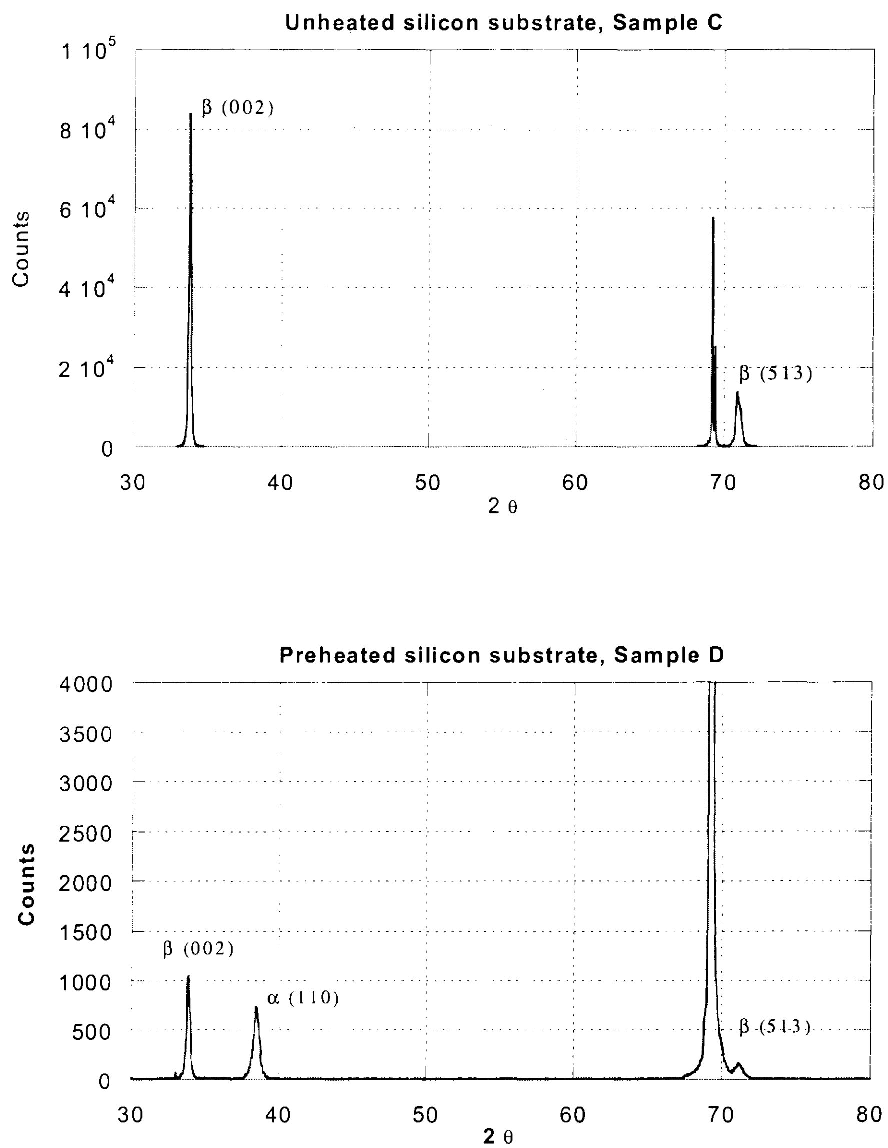

Fig 5.4 XRD data for tantalum coatings on silicon substrates, Samples C and D. This compares the unheated and the heated samples. α phase is more prominent in the heated sample.

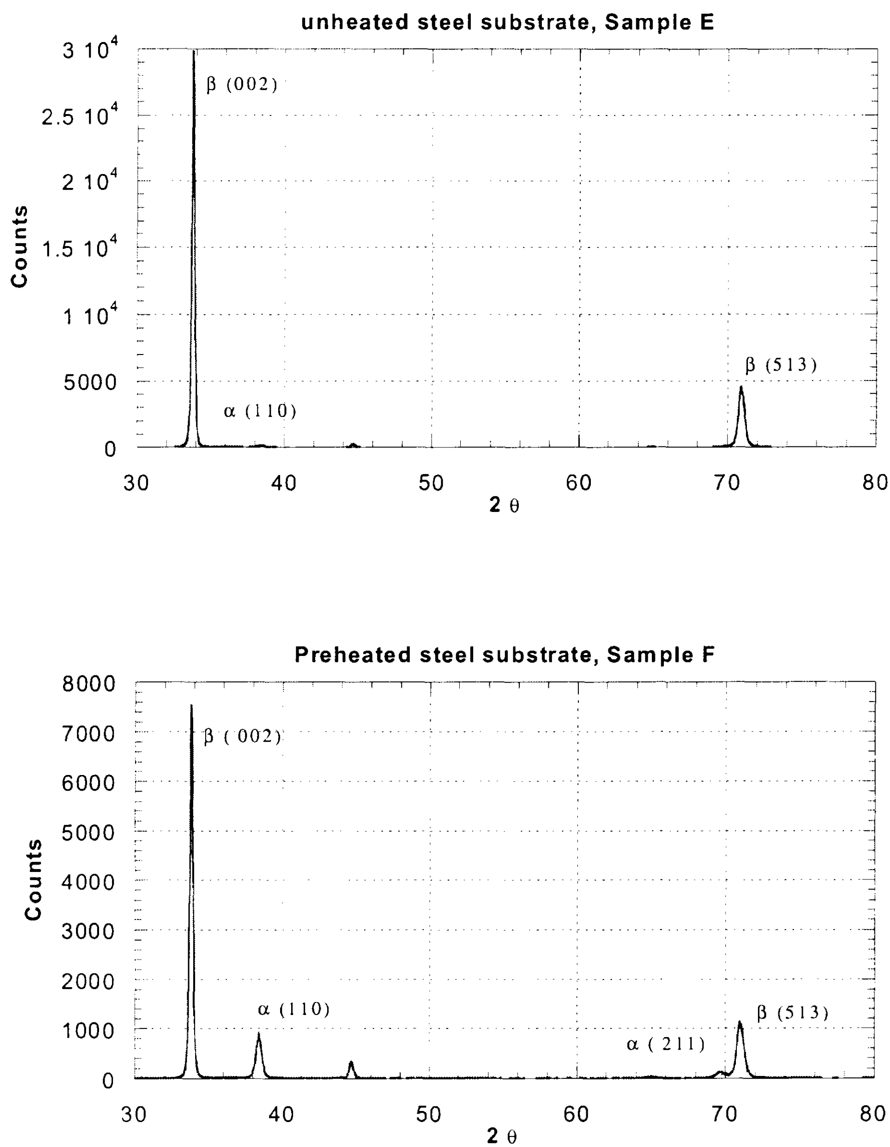

Fig. 5.5 XRD data for Tantalum coatings on unheated and heated steel substrates, Samples E and F.

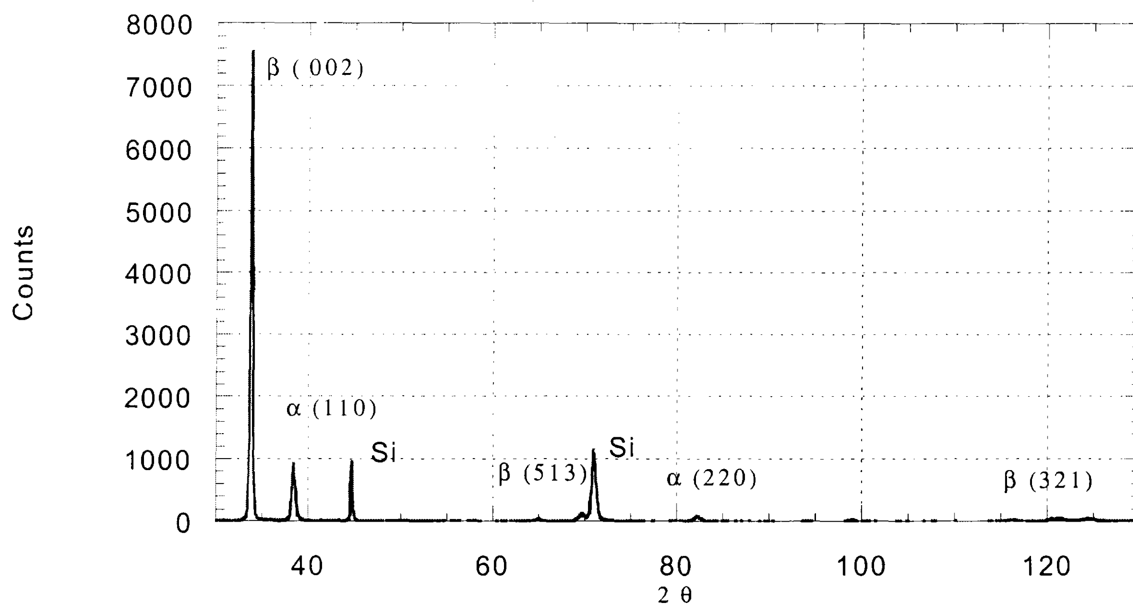

Fig. 5.6 XRD data for Tantalum coatings Silicon substrate, Sample G

5.3 X ray Fluorescence

The bulk elemental composition was acquired semi-quantitatively, using Philips PW 2400 XRF system with SemiQ software. In this study XRF was used primarily to quantify the amount of tantalum present and compare the results for samples A and B. The results for all the samples are tabulated in Table 5.2. Traces of chlorine in samples A and B may be residues of the cleaning agents used for the substrate. In XRF as X-rays are used, the depth of penetration is higher than EDX which uses electrons [52]. Also, the sensitivity of XRF is higher than EDX. The samples are seen to be of high purity Tantalum. It is seen that there is no significant difference in the impurities in both the samples.

The presence of oxygen in all the samples is most probably impurity from the sputtering chamber. The XRF results for sample G show silicon having wt. % of 12.5. This is from the substrate because the film is only ~ 2000 Å thick causing the X-rays to penetrate through it.

Table 5.2 XRF results for the samples.

Concentration in wt%, Sample no.	Tantalum	Iron	Silicon	Chlorine	Oxygen
A	99.36	0.5	-	0.14	-
B	99.07	0.44	-	0.38	-
C	91.56	-	6.39	-	2.05
D	90.32	-	8.13	-	2.76
E	90.06	7.14	-	-	2.8
F	88.62	8.61	-	-	2.76
G	86.22	-	12.62	-	1.16

5.4 Energy Dispersive X-ray Spectroscopy

The surface composition for samples A and B were determined by EDX using Kevex Sigma TM Quasar microanalyser attached to the ESEM unit. The coatings were analyzed to detect the presence of tantalum, the substrate iron, sputtering gas argon and other impurities. Calibration check was done initially using a copper foil, the main peaks of Cu were detected and the values checked. The analysis of the samples was carried out at a magnification of 2500x. The results are shown in Figure 5.7. The spectrum is found to be the same for both the samples.

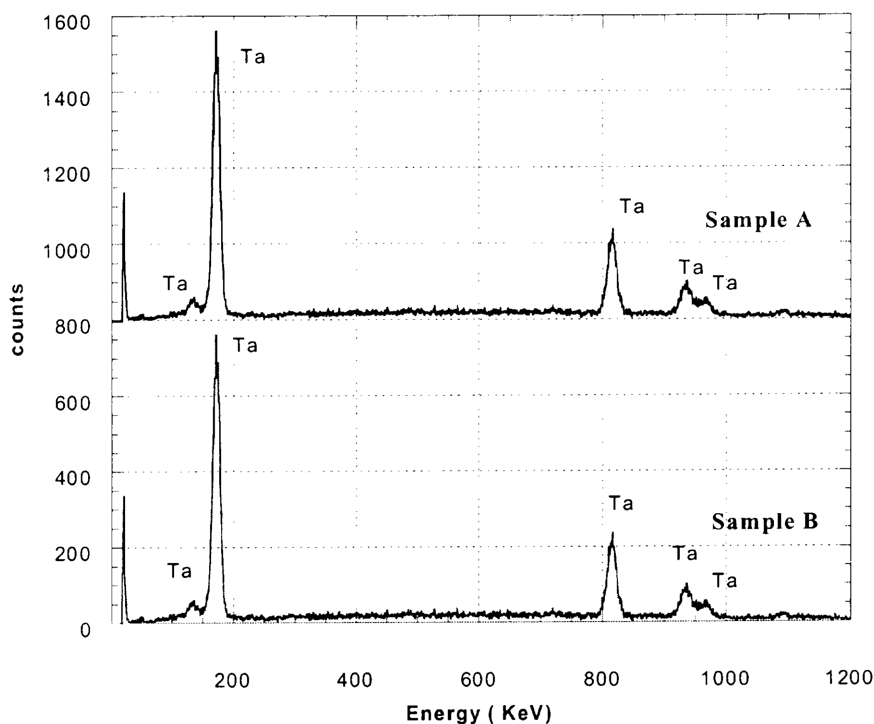

Fig. 5.7 EDX spectrum for Samples A and B.

5.5 Scanning Electron Microscopy

Electroscan 2020 model ESEM at an accelerating voltage of 20 kV was used to study the surface morphology of the two samples A and B. The emission current was 37 μAmps. Water at its vapor pressure of 5 torr is used in the chamber as a conducting medium. The samples were scanned at a magnification of 2500x. The SEM images of the are shown in fig.5.8 and 5.9, sample A which is indexed as α Ta in XRD shows a shiny finish to it, while sample B indexed as single crystal β Ta shows a distinctively different surface morphology in comparison to sample A.

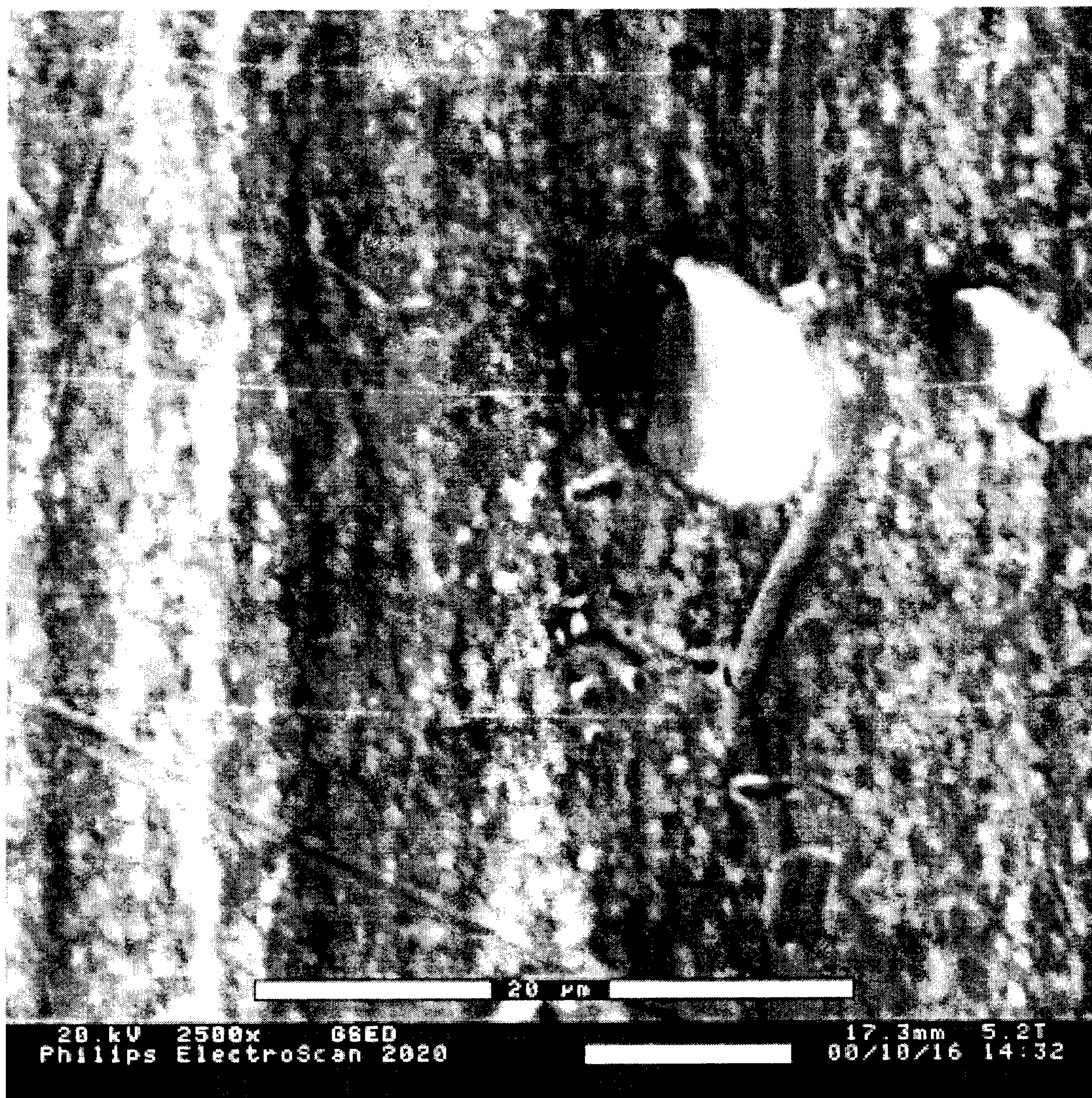

Fig. 5.8 Sample A

This scanning electron micrograph is of α Ta, as confirmed from XRD results.

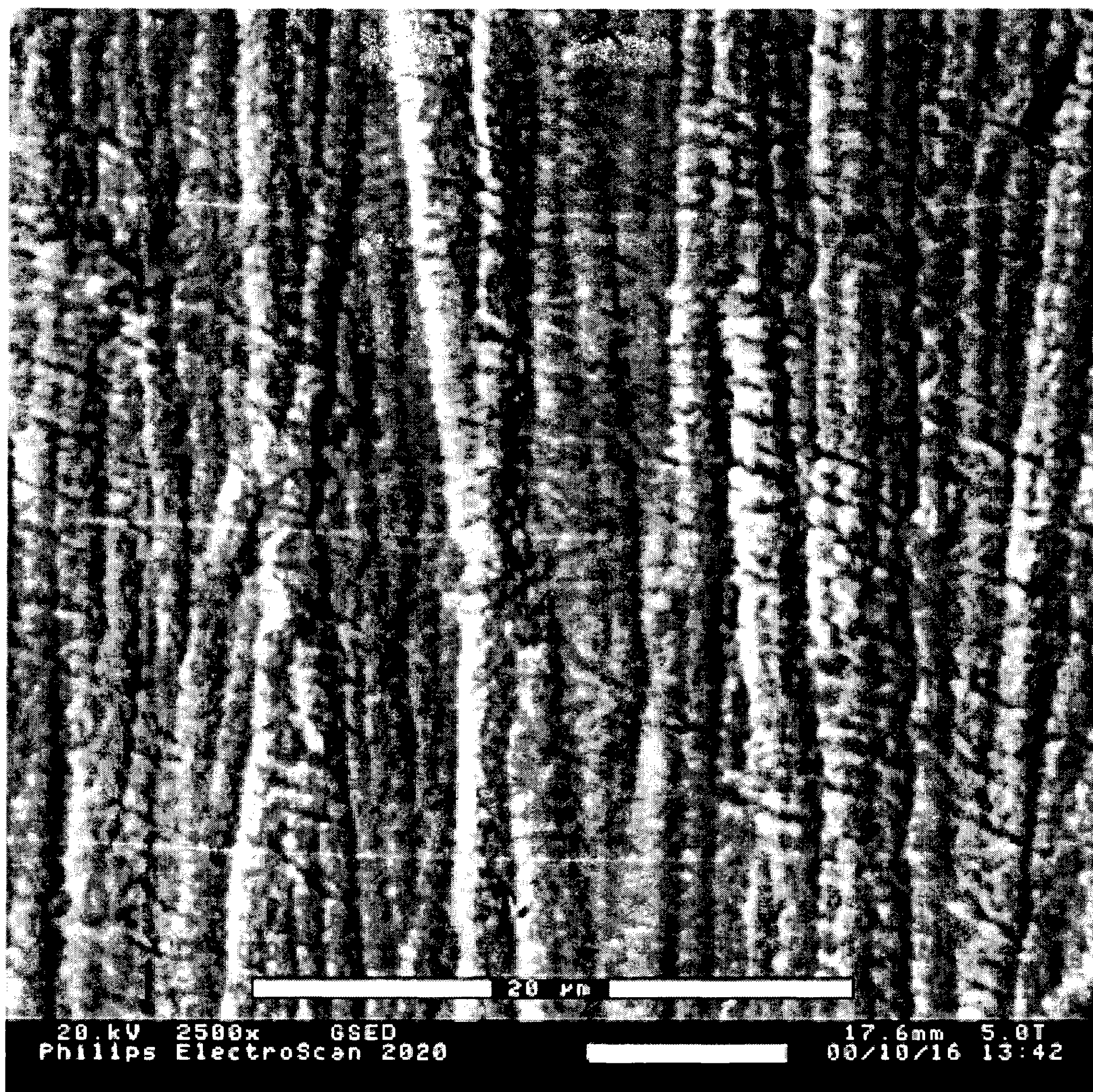

Fig. 5.9 Sample B

This scanning electron micrograph shows the β phase, the surface morphology is observed to be different than sample A.

5.6 Extended X-ray Absorption Spectroscopy

XAFS measurements were carried out for sample A and B at the National Synchrotron Light Source, Brookhaven National Laboratory, Upton, NY. The experiments were done on beam line X-11A using Si (111) double crystal monochromator. The effect of harmonics was limited by detuning the incident beam intensity by 20 %. The beam slit had dimensions of 10 mm length and ~ 1 mm width. . The experiments were done in three modes: beam incident at 45 degrees, 90 degrees and zero degrees to the sample. These modes were used to study the symmetry of the local structures. The schematic of these three modes are shown in Appendix B. These results were compared to that of tantalum foil. Data was collected at the tantalum L_{III} absorption edge (9881 eV) in all the modes. The XAFS data was analyzed using WINXAS, version 1.0 software, 1997. To obtain quantitative measurement of the average near- neighbor environment around tantalum atom, k range of 3.6315538 to 16.935499 A° was Fourier filtered to k space and fitted using theoretical spectra. The theoretical EXAFS spectra were generated using FEFF 7 codes developed by Rehr et al [23]. This analysis allows the calculation of the average coordination number, radial distances and Debye-Waller factors and higher order corrections (C3 and C_4) for shells when distorted, of atomic shells around tantalum atoms in the samples.

The theoretical model for β tantalum was generated from the model of β uranium from the work of Lawson [24]. In this work, β-Uranium is reported to have space group of $P4_2/mnm$. This model was used for the comparison studies because Moseley et al [4] on his study of electrodeposited powder sample reported that the structure of β tantalum was isomorphous with the structure of β uranium. This is a 30 atom tetragonal structure.

The x, y, z coordinates of the 30 atom tetragonal structure of β tantalum based on this model is given in Appendix C. the theoretical model for α tantalum was developed based on I*m3m* space group.

The $\chi(\kappa) * \kappa^3$ theoretical data and experimental data for α and the β phase are compared in Figure 5.10 and 5.11. It is seen that sample A has a structure similar to bcc bulk tantalum. The experimental $\chi(\kappa) * \kappa^3$ data for sample B looks similar to the generated theoretical data. The experimental and theoretical Fourier transforms are compared in Figure 5.12 and 5.13. The $\chi(\kappa) * \kappa^3$ data and fourier transforms for sample B at 45 degrees mode is compared to the data at 90 and zero degrees in Figure 5.14 and 5.15. In Figure 5.16 and 5.17, $\chi(\kappa) * \kappa^3$ data and fourier transforms for the β phase is plotted with the beam incident at 45 degrees and the calculated average of the zero and 90 degrees modes.

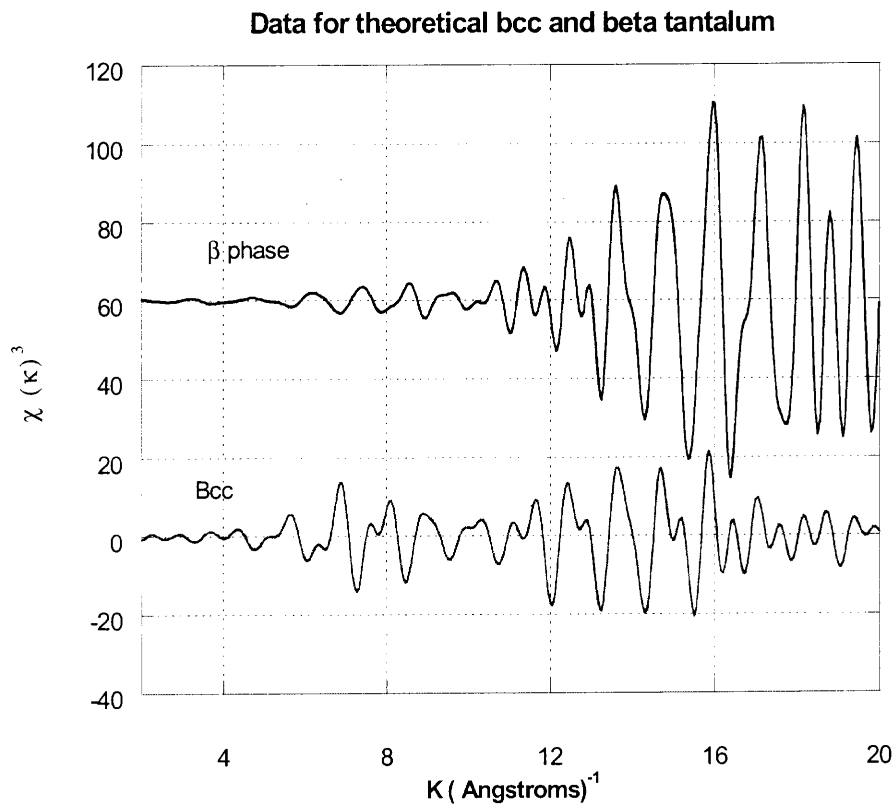

Fig. 5.10 χ (κ) * κ^3 data for the theoretical models. Debye- Waller temperature factors are not included in the calculations.

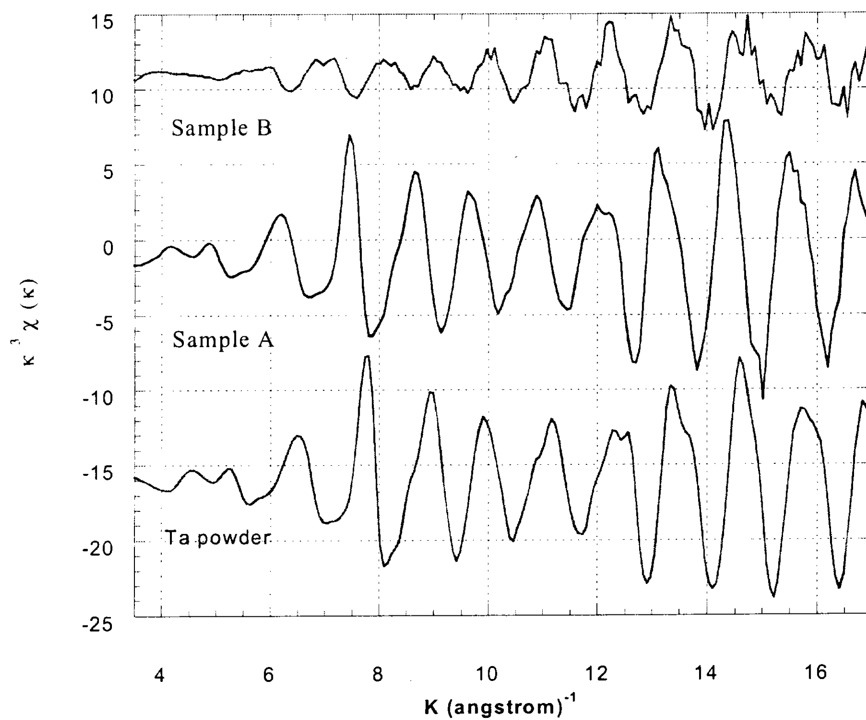

Fig. 5.11 χ (κ) * κ^3 experimental data for samples A, B compared to Ta powder. This data shows the α phase, sample A to be similar to bulk Tantalum and also, to the theoretical bcc model. While the data for the β phase, sample B is different than bulk Tantalum and matches its theoretical tetragonal model.

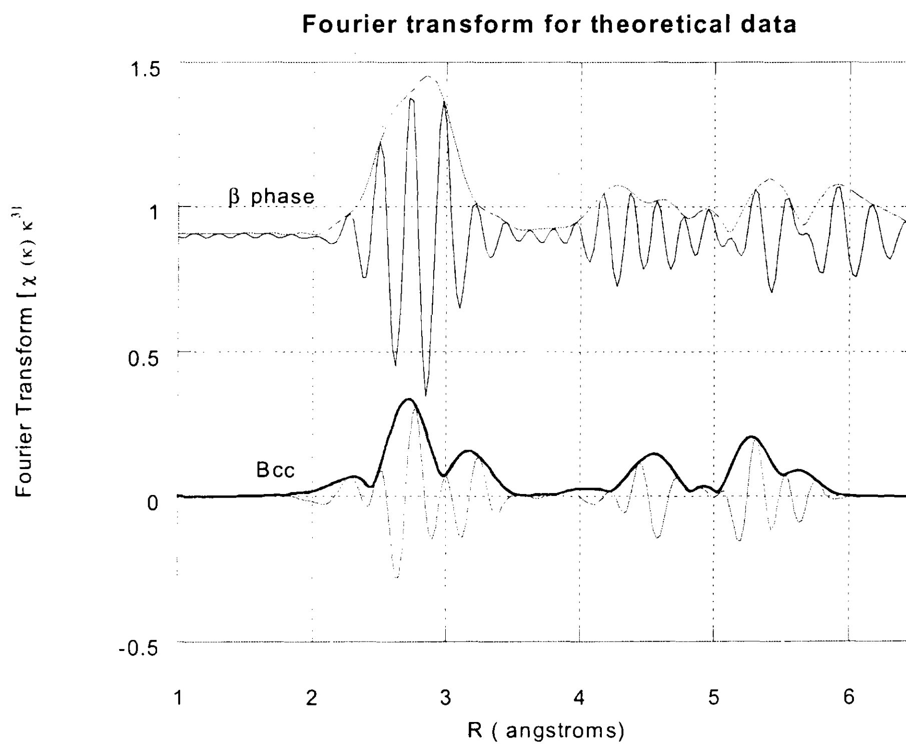

Fig. 5.12 Fourier transforms for the theoretical models for a k range of 3.0 to 16.989 A^{o-1}. Note the splitting of the main peak in the β phase.

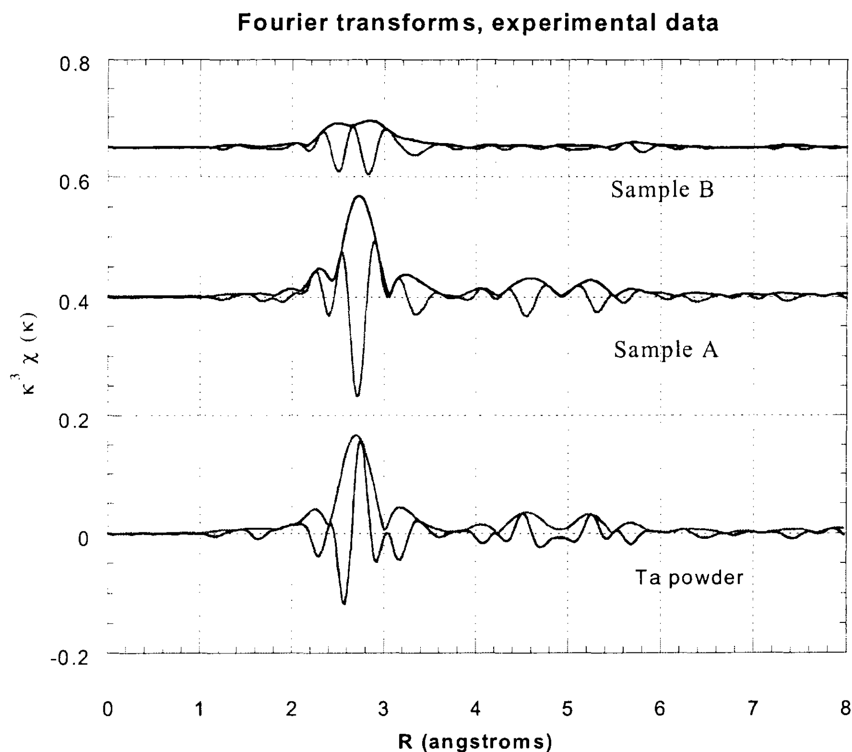

Fig. 5.13 Fourier transforms data for Tantalum powder and samples A and B of Tantalum coatings on steel substrates. This data shows that the α phase has a structure, which is similar to bulk Tantalum, and also, matches the theoretical model of bcc structure. While the experimental β phase data looks similar to its theoretical model –with a multicomponent first peak.

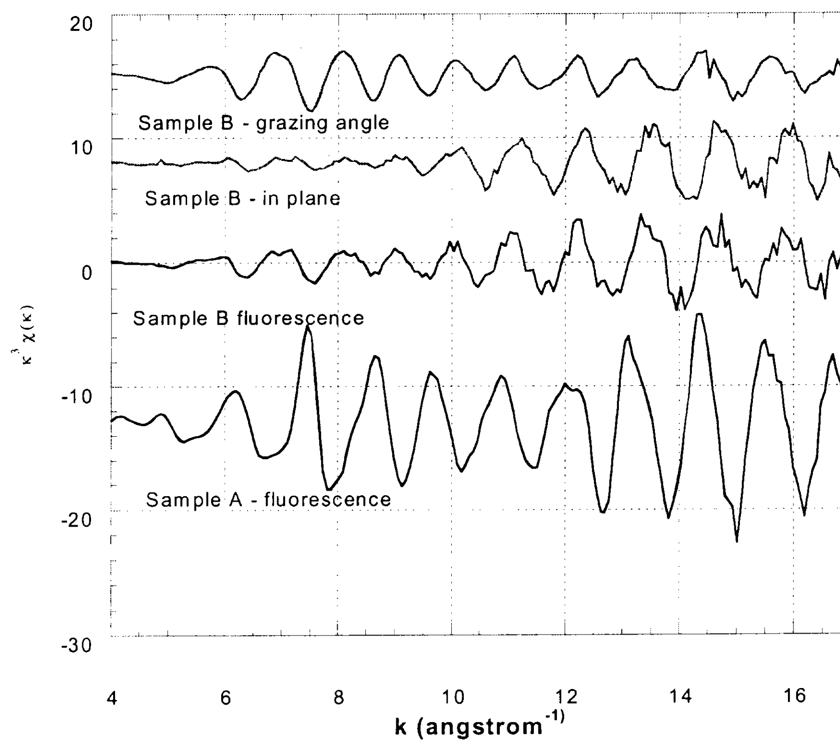

5.14 Comparison of χ (κ) * κ^3 data for the different modes of the beam for β Tantalum, sample B. This data shows that the β phase has a structure, which is asymmetrical over its coordinates, as the χ (κ) * κ^3 is different in the three modes.

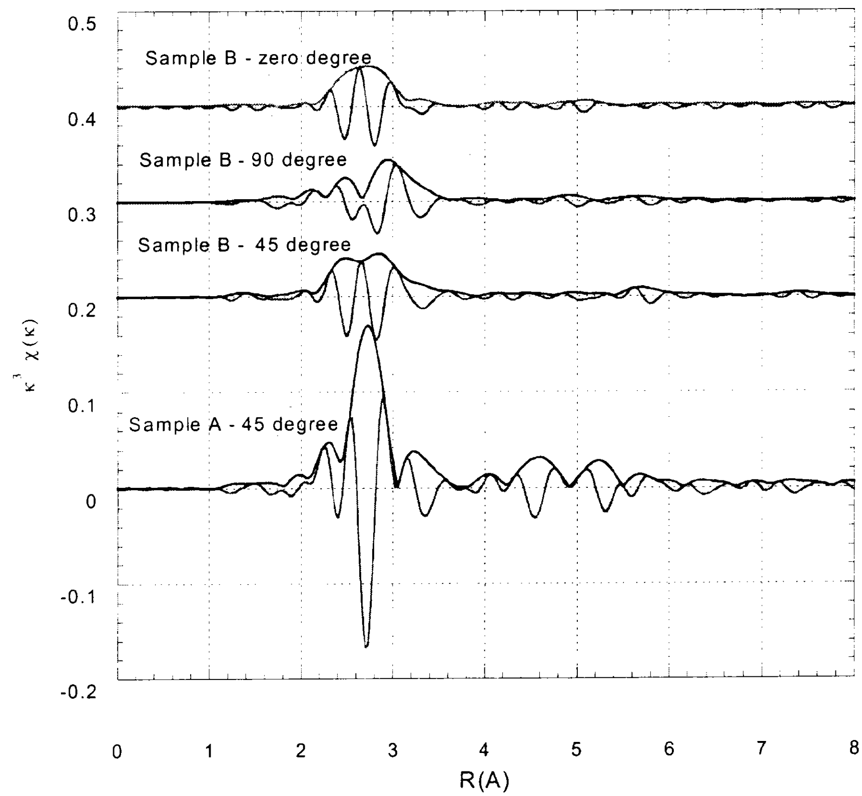

Fig. 5.15 Comparison of Fourier transforms data for the different modes of the beam for β Tantalum, sample B compared to α Tantalum, sample A.

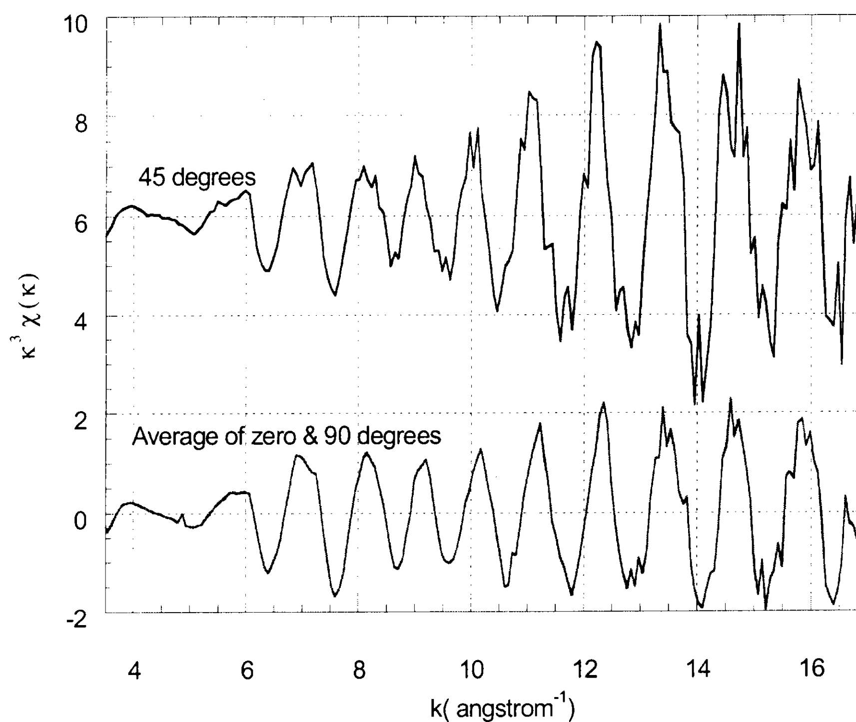

Fig. 5.16 χ (κ) * κ^3 data for the β phase, sample B with the beam incident at 45 degrees and the calculated average of the zero and 90 degrees modes. This shows the average and the 45 degrees mode data to be similar.

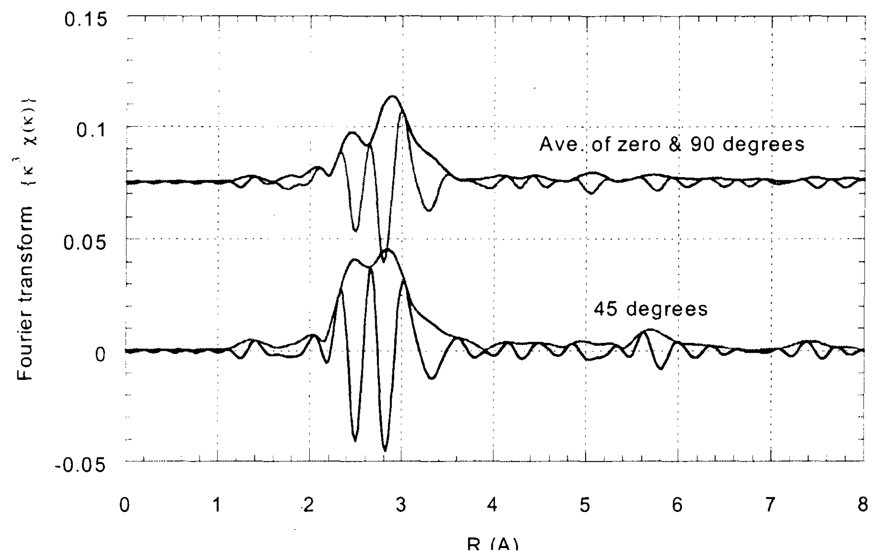

Fig 5.17 Fourier transforms data for the β phase, sample B with the beam incident at 45 degrees and the calculated average of the zero and 90 degrees modes.

5.7 TEM Analysis

TEM images and the diffraction rings where obtained at an accelerating voltage of 120 kV [57]. The initial specimen prepared from sample G showed diffraction rings of α tantalum only. Since XRD results, Fig. 5.6 showed β peaks TEM was repeated for a second specimen from the same sample to look at β phase. The diffraction spot pattern of a single grain from this specimen matched the d-spacings of β tantalum. EDX of the specimens revealed the presence of Tantalum only. Electron transparency could be obtained only at the corners of the specimen. The prepared specimens were found to be cracking during testing, which made it difficult to retest the same specimens.

The TEM images shown in Fig. 5.18 were developed at a magnification of 170,000X and are observed to have a fine grain structure. This sample had only diffraction rings of α tantalum, figure 5.20. While the TEM image shown in Fig. 5.19 obtained at a magnification of 50,000X has large grains of Tantalum. The spot diffraction pattern is of a single grain from the center of the TEM image. This is different from the alpha phase rings, and matches the d-spacings of β tantalum. This shows that this large grain structure is of β tantalum. The first strong peak of XRD corresponds to a d –spacing of 2.67 Å indexed as β (002). While the corresponding lattice spacing obtained by TEM is 3.069 Å, which is indexed as β (221). This difference in the measured values of the d – spacing by the two techniques is attributed to the sample scan area, which for TEM analysis of β tantalum is a single grain. In XRD the scan area is larger and gives the peaks averaged across the sample. The grain size was determined from the TEM images to be ~ 100-120 nm for β Tantalum while that of α Tantalum was ~ 30 – 35 nm. This shows that β Tantalum is a large grain structure in comparison to α Tantalum.

Fig. 5.18 This TEM image shows fine grain structure of α Tantalum of grain size ~30-40 nm

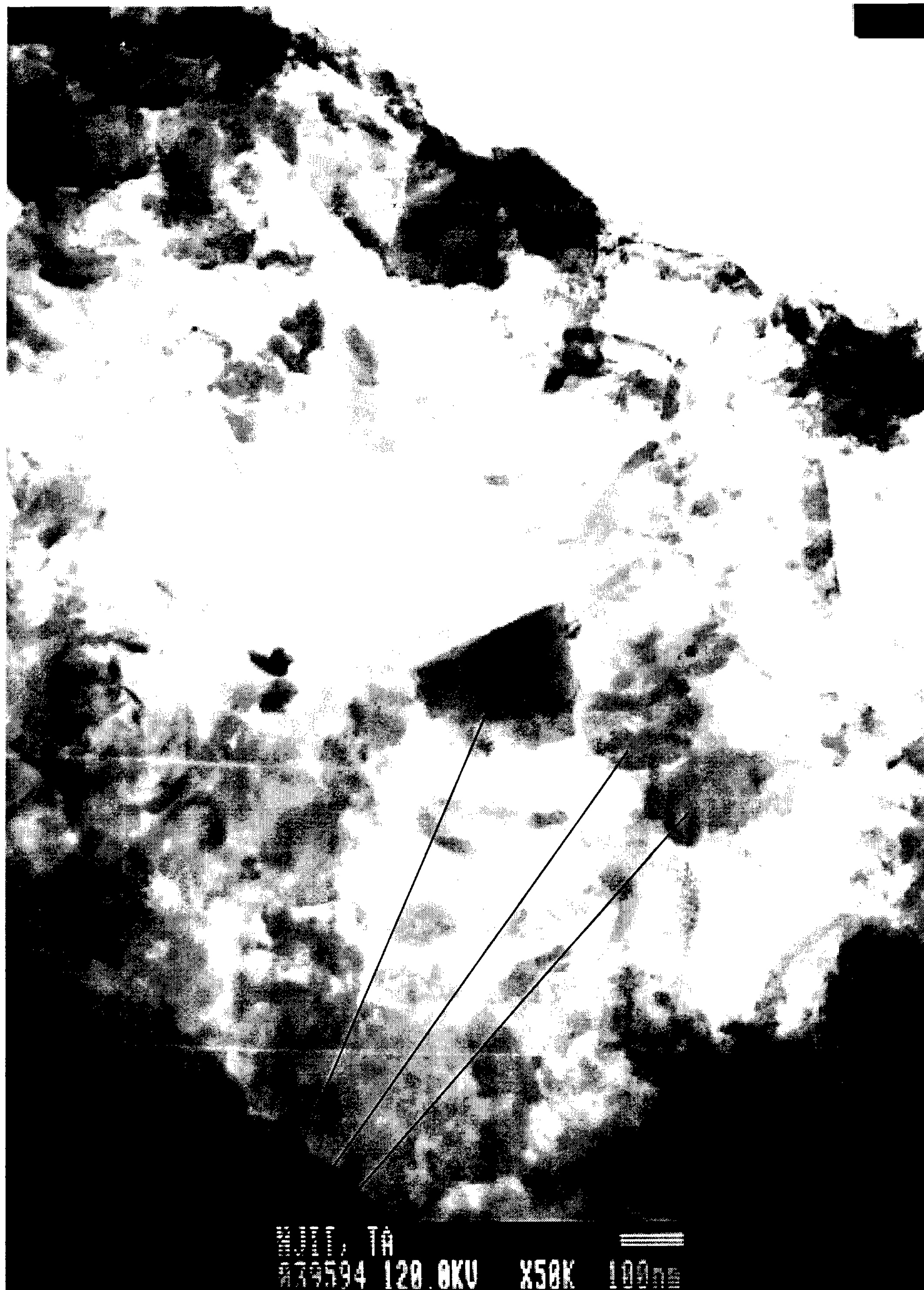

Fig. 5.19, TEM image of Ta specimen, the diffraction pattern in fig. 5.23 was obtained from the center of the image from one large grain. Grain size was measured to be ~100-120 nm.

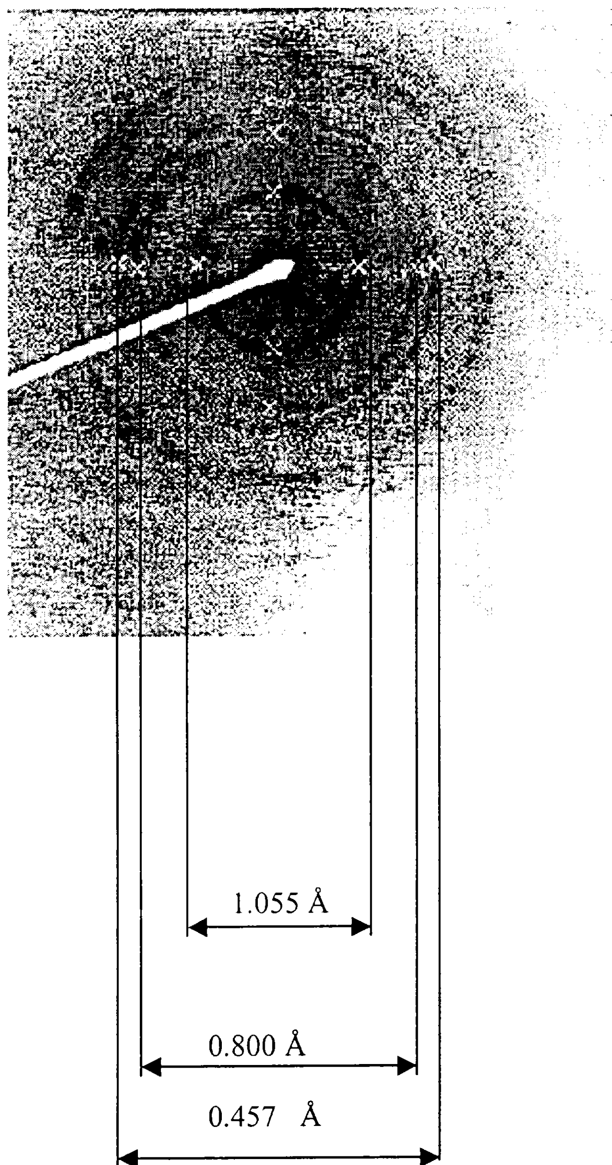

d-spacing Å	h k l
1.055	310
0.800	400
0.457	444

Fig 5.20, This Diffraction pattern of specimen shows only α Tantalum planes

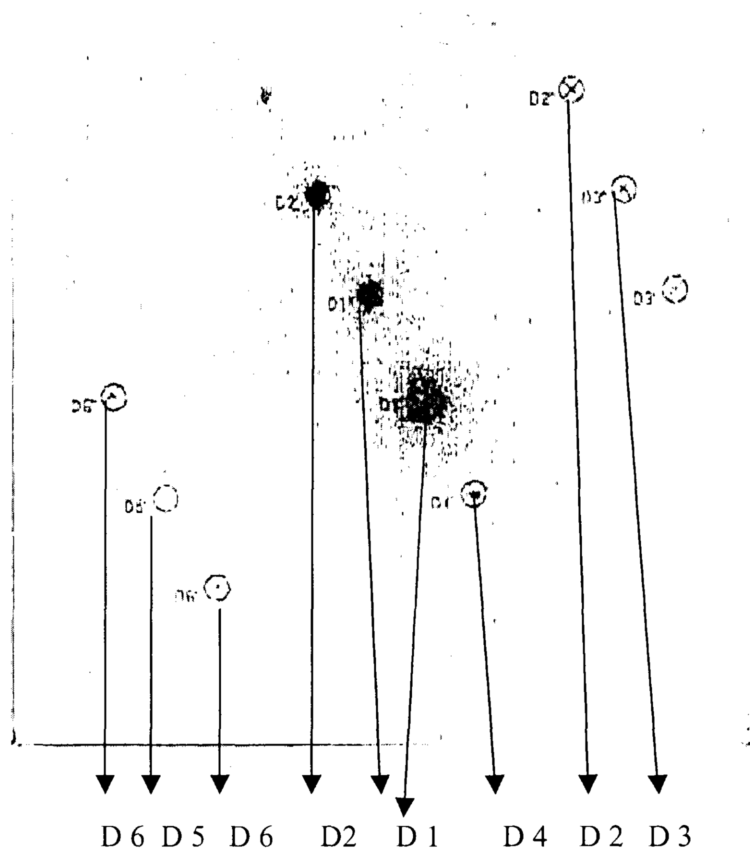

	d-spacing Å	h k l
D1	3.069	221
D2	1.222	820
D3	3.069	212
D4	3.069	122
D5	1.211	028
D6	3.132	221 or 320

Fig. 5.21 This Diffraction Spot pattern of specimen shows only β Tantalum planes. Diffraction pattern was obtained from the center of the specimen shown in the TEM image on Fig. 5.20

CHAPTER 6

DISCUSSION

6.1 X-ray Diffraction Analysis

The XRD results show the common peak of β phase to be (002). Almost all the studies of β tantalum sputtered coatings have reported it to be always preferentially oriented in the (002) plane with a *d* spacing of 2.627 Å irrespective of the type of substrate used. It is difficult to distinguish the XRD peaks of α and β as some of the major peaks of these phases overlap. The XRD peaks of α (110) plane and β (202) plane overlap at 2θ of 38.2° and d spacing of 2.35 to 2.37 Å. Also, the α tantalum (211) peak overlap β (641) at 2θ of 69°and d spacing of 1.367 Å.

The counts of the predominant β peak of (002) plane are observed to be higher than the predominant α peak (110) by a factor of 100 in almost all the samples except sample D. The lower intensity of β phase in this sample could be because of its lower percentage than the α phase in the sample. The ratio of the structure factors for these planes of β and α is calculated in Appendix C [51]. Space group *Im3m* and $P4_2/mnm$ was used for α and β tantalum respectively, for these calculations. The intensity is proportional to $|F_{hkl}|^2$ and the ratio of the intensities is also, proportional to this. The ratio of the structure factors is calculated to be 7.21, which explains the higher intensity for the β phase peak- resulting in an intensity ratio of ~50. We note that, since these films are highly textured, the measured intensity ratios will approach the theoretical limit (apart from large temperature and structure dependent Debye-Waller corrections) only if the film orientation allows to the diffracted beam to enter the detector window.

Figure 6.1 shows the (002) plane of β Tantalum and the (110) plane of α Tantalum. In the β Tantalum unit cell, 30 atoms contribute to the structure factor, while in the bcc α Tantalum, the contribution to the structure factor and hence to the intensity is only by 2 atoms in the unit cell. Thus the intensity of the (002) plane of the β phase is more than the (110) plane of the α phase, because of the contribution of 30 Ta atoms.

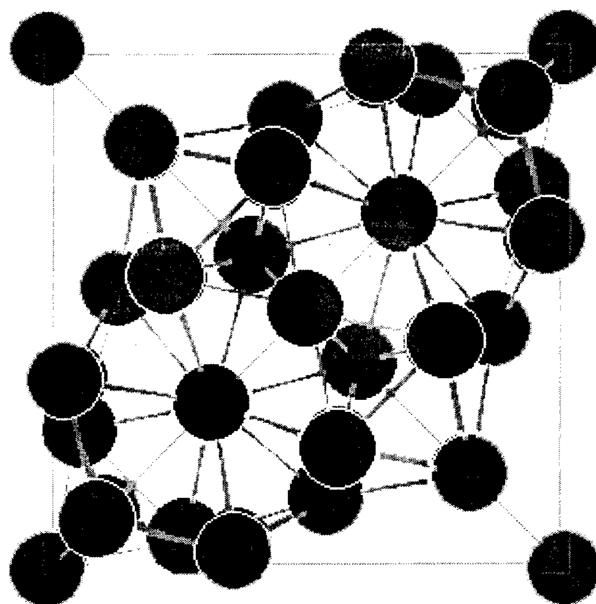

(002) plane of β Tantalum

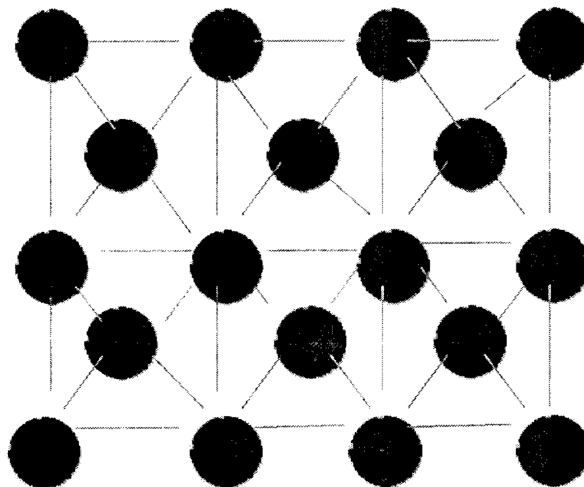

(110) plane of α Tantalum

Fig. 6.1 Main crystal planes of β and α Tantalum seen in XRD.

6.2 X-ray Fluorescence and Energy Dispersive X-ray Spectroscopy

The results of XRF and EDX do not show any significant difference in the impurities in the samples. This results matches with the study of some of the researchers. Fischer et al [27] using AES found that both the phases had the same composition but found that the phase formation depended on the substrate temperature. Catania et al [23] also, confirms this result. However other studies of the impurities of the two phases have yielded contradictory results. This difference in the impurity levels in the studies could be attributed to the different techniques and parameters used for detection of elements. Techniques better suited for the detection of lighter elements should be used to address the issue of impurities in the two phases. The results of various studies are tabulated in Table 6.1.

Read and Altman [4] investigated the purity of the two phases using emission spectroscopy; x-ray spectroscopy and xenon flash analysis. They observed that the β tantalum films were purer than the α tantalum films. Hieber and Lautenbacher's [32] studies concluded that the α tantalum films were purer. Das [10] using ion probe microanalysis found that β tantalum had about five times more nitrogen in it than α. Rottersman and Bill [21], and Stavrev et al [44] by Auger Electron Spectroscopy (AES) found that β tantalum contained a maximum of 4 at. % nitrogen. As the nitrogen content was increased in the sputtering chamber the α phase was formed. Schwartz and Feit [39] based on their studies of the residual gases during sputtering process concluded that an 'X' impurity prevented the formation of β tantalum and induced the formation of the α phase. However this presence of impurities for the formation of β tantalum is not seen in this study.

Table 6.1, The composition of the two phases having impurities, as determined by researchers

	α phase	β phase	Operating parameters
Read [8]	0.17%wt N	0.07% wt N	Ar gas = 5 sccm Base pr. 2 x 10^{-6} torr
Fischer [27]	-	-	P = 500 W Ar = 5 sccm, difference in temperature of substrates
Stavrev [44]	4% at N	-	P = 1000 W Ar = 5 sccm N = 0-5 sccm O = 0-5 sccm
Das [10]	-	N_2	Not mentioned
Schwartz [39]	N_2 or O_2	-	Ar = 20 sccm Base pr. 4 x 10^{-6} torr
Catania [23]	1.5-2% wt Ar	1.5-2% Ar	Ar = 10 sccm
Schauer [22]	-	N_2 or O_2	Base pr. 10^{-8} torr
This work Sample A & B	0.14 –0.4 % wt. Cl	0.14 –0.4 % wt. Cl	Not known
Samples C, D,E,F & G	1.2 to 2.8 % wt O_2	1.2 to 2.8 % wt O_2	Ar = 12 sccm Base pr. 1 x 10^{-7} torr

6.3 Scanning Electron Microscopy

Sample, A which is indexed as having predominantly, α peaks shows step growth and has a shiny finish to it, while sample B having pure β peaks shows a preferred orientation in its surface morphology in comparison to sample A.

SEM images in reference [11, 17, 32] of the β phase show it to be having columnar growth and preferred orientation. Also, AFM images obtained by Fischer et al [27] showed the β phase to have preferred orientation and texture. While the

AFM images in the study by Stavrev et al [44] showed the β phase to be of polycrystalline circular grains. The α phase has also, been reported to have a columnar structure in the work of Chen et al [37] and Mammana et al [47], which is not seen in this study.

6.4 Transmission Electron Microscopy

The TEM images of different areas of the same sample show the grain size of the α phase to be four times smaller than that of the β phase. The phases were identified by their electron diffraction patterns. Other researchers in their studies have also, seen this difference in the grain sizes for the two phases. The grain sizes seen in different studies are tabulated in Table 6.2.

The results of the grain sizes closely match the results obtained by Stavrev [44]. He calculated the grain sizes from the width of the XRD peaks. Lautenbacher et al [32] observed an electron diffraction pattern for a β tantalum sample corresponding to (330) and (411) planes. TEM image of α tantalum in Heiber et al 's [24] work shows it to be randomly oriented and having a coarse grain structure whereas the TEM image of β tantalum showed it to be preferentially oriented and having a fine grain structure. He also, observed α tantalum to have smaller grain sizes and β tantalum was made up of larger grains. This is also, observed in this work. Face and Prober's [38] TEM work on β tantalum showed it to be randomly oriented and having grain sizes of 30 nm which were almost twice that of α tantalum. Kee- Won et al [36] in a high resolution electron microscopy [HREM] study of β tantalum found it to be composed of nanoscale columnar grains of 9 nm in size. The electron diffraction showed d spacing corresponding to (002) plane only. Mills [11] determined the grain sizes of β and α Tantalum to be 35 nm and

12.5 nm respectively. These dimensions were determined from X-ray studies. Sajovec et al [45], however, measured α tantalum and β tantalum to have grain sizes of 15 nm and 6 nm respectively. The TEM diffraction pattern had rings of (104), (206), (101) and (004), while the XRD pattern had (002) and (304) planes of β tantalum. This difference in the observed planes in the two techniques or the difference in grain sizes is not clarified. Das [10] in his work on electron microscopy of α and β samples observed diffraction rings for the β phase. This showed d –spacing of 2.56 Å with an indexing of (400). XRD pattern had a strong (002) peak. having d- spacing of 2.67 Å. This difference in the d-spacing values in the two methods was attributed to the substrate stress. This difference is also, noticed in this study. He also, observed that higher voltages were required to detect the innermost rings for β tantalum, as at lower voltages the inner rings were not distinct.

Table 6.2,Grain sizes of the two phases of Tantalum as seen in various TEM studies

	Grain size of α phase, nm	Grain size of β phase, nm	Method used to determine grain size
Mills [11]	12.5	35	TEM
Sajovec [49]	15	7.9	TEM
Face [38]	15	30	TEM
Kee Won [36]	-	9	HREM
Stavrev [44]	10	90	XRD
This work	30	120	TEM

6.5 Extended X-ray Absorption Spectroscopy

The χ (κ^3) experimental data of the samples A and B compared to the theoretical data of α and the β phase shows sample A to have a structure similar to bcc bulk tantalum. The experimental χ (κ^3) data for sample B looks similar to the generated theoretical model for

the β phase. The Fourier transforms of β phase, sample B shows it to be a highly disordered structure and having a multi component first shell, which is different from the bcc structure. The Fourier transform of this phase also, looks similar to that of the theoretical model. The χ (κ^3) data and fourier transforms data for β tantalum at 45 degrees mode in comparison to the data at 90 and zero degrees shows the structure of this phase to be asymmetrical over its coordinates that is different from the bcc structure. χ (κ) * κ^3 data and fourier transforms for the β phase plotted with the beam incident at 45 degrees and the calculated average of the zero and 90 degrees modes shows the average and the 45 degrees mode data to be similar.This results shows that β tantalum has a local structure which is different from the bcc structure. Also, the local structure of this phase is found to be similar to that of β Uranium having a space group of $P4_2/$ *mnm* having a 30 atom unit cell.

6.6 Discussion on Films Deposited on Preheated Substrates

The XRD results of preheated samples D and F show them to have a higher percentage of α phase than the unheated samples C and E, figure 5.4 and 5.5. These results have also, been observed in other studies. However, most of the studies have been carried out by heating the substrate during deposition process- which was not done here. Our study thus represents sample precleaning –removal of adsorbed impurities.

The formation of the stable α phase could be similar to the mechanism of formation of an epitaxial layer on a substrate, which requires the surface to be of very high purity. The formation of a mixture of α and β phases when the substrates are heated may be because of the removal of adsorbed layers form the surface of the substrates, which enhances the formation of the α phase. Epitaxial layer requires high temperatures

and low deposition rates for its formation as these conditions allows for high surface migration rates for the deposited atoms, which are adsorbed on the surface. This higher mobility of the adatoms allows them to reach stable positions and thus, form a monocrystalline layer. The presence of impurities on the surface can impede the motion of the atoms and produce a stacking fault or defects. The suppression of adatom migration during growth can cause the deposition of a polycrystalline film. The formation of the stable α phase may be induced by this same mechanism wherein at higher substrate temperatures the mobility of tantalum adatoms on cleaner substrates leads them to more energetically stable positions. At lower temperatures, the surface migration rate is lower, which impedes the positioning of the adatoms at energetically favorable sites; this mechanism may be one of the causes for the formation of β phase.

CHAPTER 7

CONCLUSIONS

The purpose of this study was to characterize the two main phases of tantalum. The required phase for this application is α, consequently this study may help in the differentiation of phases in the sputtered samples. The conclusions drawn from this work are:

- XRD measurements of β tantalum show a predominant (002) peak with respect to a tetragonal cell. This has been seen in most studies of the β phase reported in literature. The intensity of this peak in pure sputtered β tantalum sample is much higher than the (110) peak seen in pure α tantalum for the same sample volume. This is in agreement with structure factor calculations which gives a β (002) to α (110) intensity ratio of ~ 50.
- The EDX and XRF results, for the samples do not reveal any differences in the level of impurities found in the two tantalum phases. However,, techniques better suited for the detection of lighter elements should be used to confirm this finding for lower atomic mass impurities.
- The β phase is seen to have a grain size of 100-120 nm in TEM analysis, which is about 4 times that of the α phase. This confirms the observations of other researchers.
- EXAFS analysis shows the local structure of β phase to be consistent with that of β Uranium (space group $P4_2/mnm$). The coordination of Ta atoms in the β phase is not isotropic.
- Experiment on the heated substrates suggests that the formation of the phases is dependent on the surface condition of the substrates.

APPENDIX A

The three modes of experiments done in XAFS.

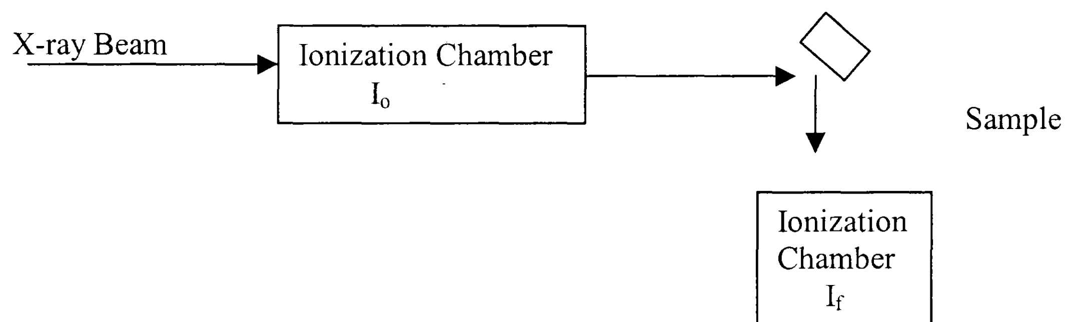

Fig A1 Schematic for XAFS experiment in fluorescence mode at 45 degrees

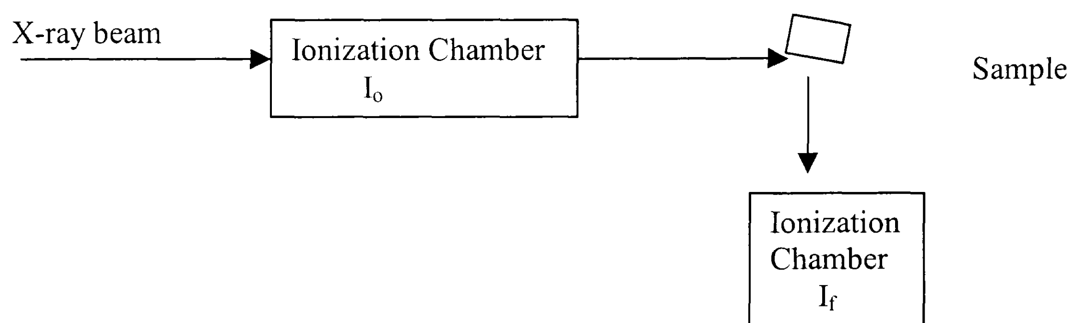

Fig A2 Schematic for XAFS experiment with beam at grazing angle mode (zero degrees) to the sample.

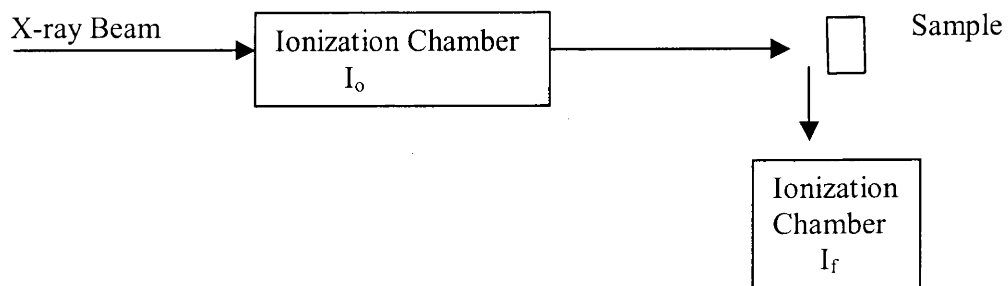

Fig A3 Schematic for XAFS experiment with beam in plane (ninety degrees) to the sample.

APPENDIX B

The lattice constants and x,y,z coordinates of β tantalum generated from β Uranium [25, 50]:

Space group: $P4_2/mnm$

a = 10.194 A°
c = 5.313 A°

Atom type	x	y	z
Ta	0	0	0.5
Ta	.5	.5	0
Ta	.103	.103	0
Ta	.603	.397	.5
Ta	.897	.897	0
Ta	.397	.603	.5
Ta	.3188	.3188	.7444
Ta	.6812	.6812	.7444
Ta	.8188	.1812	.2444
Ta	.1812	.8188	.2444
Ta	.6812	.6812	.2556
Ta	.3188	.3188	.2556
Ta	.1812	.8188	.7556
Ta	.8188	.1812	.7556
Ta	.5622	.2343	0
Ta	.2343	.5622	0
Ta	.0622	.2657	.5
Ta	.7343	.9378	.5
Ta	.4378	.7657	0
Ta	.7657	.4378	0
Ta	.9378	.7343	.5
Ta	.2657	.0622	.5
Ta	.3655	.0391	0
Ta	.0391	.3655	0
Ta	.8655	.4609	.5
Ta	.5391	.1345	.5
Ta	.6345	.9609	0
Ta	.9609	.6345	0
Ta	.1345	.5391	.5
Ta	.4609	.8655	.5

APPENDIX C

The structure factor for different crystal structures depends on the number of atoms in the unit cell. The intensity that is observed for any Bragg reflection is proportional to the structure factor $|F_{hkl}|^2$. From the position of the atoms in the unit cell (x, y, z) the structure factor can be calculated The structure factor, divided by f_{Ta} the atomic scattering factor, is given by:

$$F_{hkl} := \sum_{n=1}^{nu} e^{2\cdot\pi\cdot i\cdot\left(h\cdot H_{n,1}+k\cdot H_{n,2}+l\cdot H_{n,3}\right)}$$

Where hkl are the indices of the plane under consideration, n is the number of atoms in the unit cell. In this calculations β (002) and α (110) are considered. H in the calculations below is the x y z coordinates of β tantalum as listed in Appendix B. nu denotes the number of atoms in the unit cell of β tantalum, which is 30.

Structure Factor calculations for β and bcc Tantalum (divided by f_{Ta} the atomic scattering factor)

Calculations were done using Mathcad.

$h := 0$

$k := 0$

$l := 2$

$i := \sqrt{-1}$ *

$nu := 30$

$$H := \begin{bmatrix} 0 & 0 & 0.5 \\ 0.5 & 0.5 & 0 \\ 0.10 & 0.10 & 0 \\ 0.60 & 0.39 & 0.5 \\ 0.89 & 0.89 & 0 \\ 0.39 & 0.60 & 0.5 \\ 0.318 & 0.318 & 0.744 \\ 0.681 & 0.681 & 0.744 \\ 0.818 & 0.181 & 0.244 \\ 0.181 & 0.818 & 0.244 \\ .681 & .681 & .255 \\ .318 & .318 & .255 \\ .181 & .818 & .755 \\ .818 & .181 & .755 \\ .562 & .234 & 0 \\ .234 & .562 & 0 \\ .062 & .265 & .5 \\ .734 & .937 & .5 \\ .437 & .765 & 0 \\ .765 & .437 & 0 \\ .937 & .734 & .5 \\ .265 & .062 & .5 \\ .365 & .039 & 0 \\ .039 & .365 & 0 \\ .865 & .460 & .5 \\ .539 & .134 & .5 \\ .634 & .960 & 0 \\ .960 & .634 & 0 \\ .134 & .539 & .5 \\ .460 & .865 & .5 \end{bmatrix}$$

$$F_{002} := \sum_{n=1}^{nu} e^{2\cdot\pi\cdot i\cdot\left(h\cdot H_{n,1}+k\cdot H_{n,2}+l\cdot H_{n,3}\right)}$$

$F_{002} = 14.0$

For bcc Tantalum (110) we have:

$h := 1$
$k := 1$
$l := 0$
$i := \sqrt{-1}$
$num := 2$
$e^{2 \cdot \pi \cdot i \cdot (h \cdot 0 + k \cdot 0 + l \cdot 0)} = 1$
$e^{2 \cdot \pi \cdot i \cdot (h \cdot .5 + k \cdot .5 + l \cdot .5)} = 1$
$F_{110} = 2$

Hence, the ratio $|F_{\beta 002} / F_{\alpha 110}|$ is 7.01

REFERENCES

1. ASM Metals handbook, desk edition, Chap. 4, 1985.

2. ASM Metals Handbook, Properties of pure metals, pp. 724, 803-804, Vol. 2, 1985.

3. Erik Jonathan Weiss, "Preliminary ecological risk assessment to assess the implications of replacing chromium plating with tantalum coatings," *MS thesis*, Department of Environmental Engineering, New Jersey Institute of Technology, Newark, New Jersey, 1999.

4. P T Moseley, C. J. Seabrook, "The Crystal Structure of Beta Tantalum", *Acta Crystallogr* Sec. B, 29, pp. 1170-1171, 1973.

5. J. F. Thompson, M. D. Miller, "X-ray Diffraction Analysis of Electrodeposited Beta Tantalum", *Rept. No. ARCOB- TR- 93031,* 1993.

6. A J Perry, C Beguin, H E Hintermann, "The microstructure of Tantalum coatings on mild steel," *Proceedings of the 3rd European Conference on Chemical Vapor Deposition*, Neutachel, Switzerland, pp. 131-139, April 1980.

7. Prabha Shivaramkrishnan, "Characterization of Tantalum Coatings on Steel," *MS Thesis*, Department of Materials Science and Engineering, New Jersey Institute of Technology, Newark, New Jersey, 1999.

8. M.H Read, C. Altman, " A New Structure in Tantalum Thin Films," *Applied Physics Letters*, Vol.7, No.3, pp. 51-52, 1965.

9. D W Matson, M D Mertz, E D McClanahan, " High rate sputter deposition of wear resistant tantalum coatings," *Journal of Vacuum Science and Technology,* Vol. A, 10(4), pp. 1791-1796, 1992.

10. G. Das, " New Structure of Sputtered Tantalum," *Thin Solid Films,* Vol. 12, pp. 305-311, 1972.

11. D Mills, "The structure of sputtered tantalum," *Journal of Canadian Ceramic Society*, 35, pp. 48-52, 1965.

12. R. D. Burbank, "An X-ray study of Beta Tantalum," *Appl. Cryst.*, 6, 217, 1973

13. W D Westwood, "The influence of conducting underlays on the properties of sputtered tantalum films," *Thin Solid Films*, Vol. 6, pp. 307-320, 1970.

14. Milton Ohring, *The materials science of thin films*, chapters 3, 5, 6; Academic Press, CA, 1992.

15. Stanley Wolf, Richard N Tauber, *Silicon processing for the VLSI era*, Vol. 1, chapter 11, second ed., Lattice press, CA, 1999.

16. Kurt J. Lesker company catalogue, *Magnetron sputter deposition sources*, pp.1.

17. A Schauer, W Peters, W Juergens, "A very pure thin film tantalum phase," *Thin Solid Films*, Vol. 8, pp. R9- R12, 1971.

18. L G Feinstein, R D Huttemann, " Factors controlling the structure of sputtered Ta films," *Thin Solid Films*, Vol. 16, pp. 129-145, 1973.

19. Shigehiko Sato, " Nucleation properties of magnetron-sputtered tantalum," *Thin Solid Films*, Vol. 94, pp. 321-329, 1982.

20. R Hoogeveen, M Moske, H Geisler, K Samwer, " Texture and phase transformation of sputter-deposited metastable Ta films and Ta/Cu multilayers," *Thin Solid Films*, Vol. 275, pp. 203-206, 1996.

21. M H Rottersman, M J Bill, " Properties of planar-magnetron-sputtered tantalum films," *Thin Solid Films*, Vol. 61, pp.281-288, 1979.

22. A Schauer, M Roschy, " RF sputtered β-tantalum and bcc tantalum films," *Thin Solid Films*, vol. 12, pp. 313-317, 1972.

23. Philippe Catania, Ronnen A Roy, Jerome J Cuomo, " Phase formation and microstructure changes in tantalum thin films induced by bias sputtering," *Journal of Applied Physics*, Vol. 74(2), pp.1008-1014, 1993.

24. K Hieber, N M Mayer, "Structural changes of evaporated tantalum during film growth," *Thin Solid Films*, Vol. 90, pp. 43-50, 1982.

25. J J Rehr, J Mustre de Leon, S I Zabinski, R C Albers, " Theoretical X-ray absorption fine structure standards," *Journal of American Chemical Society*, Vol. 113, pp. 3676-3678, 1991.

26. A C Lawson, C E Olsen, "Structure of β- Uranium", *Acta Cryst.*, B44, pp. 89-96, 1988.

27. D. Fischer, O. Meissner, B. Bendjus, J. Schreiber, M. Stavrev, C. Wenzel, "AFM Characterization of Ta-based Diffusion Barriers for Use in Future Semiconductor Metallization", *Surface and Interface Analysis*, Vol. 25, pp. 522-528, 1997.

28. L G Feinstein, D Gerstenberg, "Structure and Electrical Properties of Ta Films Sputtered in Ar-O_2", *Thin Solid Films*, Vol. 10, pp.79-89, 1972.

29. S L Lee, M Cipollo, D Windover, C Rickard, "Analysis of Magnetron-Sputtered Tantalum Coatings versus Electrochemically Deposited Tantalum from Molten Salt", *Surface and Coatings Technology*, 120- 121, pp. 44-52, 1999.

30. S L Lee, D Windover, " Phase, residual stress, and texture in triode-sputtered tantalum coatings on steel," *Surface and Coatings Technology*, 108-109, pp. 65-72, 1998.

31. W D Westwood, N Waterhouse, P S Wilcox, *Tantalum thin films*, Academic Press, London, 1975.

32. K Heiber, E Lautenbacher, "Stabilization of sputtered β-tantalum by a tantalum silicide interlayer," *Thin Solid Films*, Vol. 66, pp. 191-196, 1980.

33. Grant Bunker, *Elements of X-ray Absorption Spectroscopy*, Physics Department of Illinois Institute of Technology, Chicago, IL.

34. Boon K Teo, *Extended X-ray Absorption Fine Structure Spectroscopy: Basic Principles and Data Analysis*, Chapters 2-6, Springer-Verlag, NY, 1985.

35. P N Baker " Preparation and properties of tantalum thin films," Invited review, *Thin Solid Films*, Vol. 14, pp. 3-25, 1972.

36. Kee- Won Kwon, Changsup Ryu, Robert Sinclair, S Simon Young, "Evidence of heteroepitaxial growth of copper on β tantalum," *Applied Physics Letters*, 71(21), pp.3069-3071, 1997.

37. G S Chen, P Y Lee, S T Chen, " Phase formation behavior and diffusion barrier property of reactively sputtered tantalum-based thin films used in semiconductor Metallization," *Thin Solid Films*, Vol. 353, pp. 264-273, 1999.

38. D W Face, D E Prober, "Nucleation of body – centered-cubic tantalum films with a thin niobium underlayer," *Journal of Vacuum Science and Technology A,* Vol.5, No. 6, pp.3408-3411, 1987.

39. N Schwartz, E D Feit, "Impurity effects in the nucleation of alpha (bcc) – tantalum or β –tantalum films," *Journal of Electrochemical Society*, Vol. 124, No. 1, pp. 123-131,1976.

40. PCDFWIN Software, JCPDS, International Centre for Diffraction data (ICDD), 1996.

41. Philip Catania, James P Doyle, Jerome J Cuomo, " Low resistivity body-centered cubic tantalum thin film as diffusion barriers between copper and silicon," *Journal of Vacuum Science and Technology A*, Vol. 10, No.5, pp.3318-3321, 1992.

42. L G Feinstein, R D Huttemann, " Annealing and phase stability of tantalum films," *Thin Solid Films*, vol. 16, pp. 104-114, 1973.

43. M H Read, D H Hensler, " X-ray analysis of sputtered films of beta-tantalum and body centered cubic tantalum," *Thin Solid Films*, Vol. 10, pp.123-125, 1972.

44. Momtchil Stavrev, Dirk Fischer, Christian Wenzel, Kurt Drescher, Norbert Mattern, " Crystallographic and morphological characterization of reactively sputtered Ta, Ta-N and Ta-N-O thin films," *Thin Solid Films*, Vol. 307, pp. 79-88, 1997.

45. F Sajovec, P M Meuffels, T Schober, " Structural and electrical properties of ion beam sputter deposited tantalum films," *Thin Solid Films*, Vol. 219, pp. 206-209, 1992.

46. L A Clevenger, A Mutscheller, J M E Harper, C Cabral Jr., K Barmak, " The relationship between deposition conditions, the beta to alpha phase transformation, and stress relaxation in tantalum thin films," *Journal of Applied Physics*, Vol. 72 (10), pp. 4918-4924, 1992.

47. P Mammana, I L Torriani, M A Silveria, L A C de Almeida, " Characterization of Ta thin films obtained by dc sputtering," *Vacuum*, Vol. 41 (4-6), pp. 1403-1404, 1990.

48. John P Silbilia, *A guide to materials characterization and chemical analysis*, 2 ed., pp. 143-165, VCH publishers, NY, 1996.

49. Eric Lifshin, Materials Science and Technology, *Characterization of Materials*, Vol. 2A, part 1, VCH publishers, NY, 1992.

50. V P Belevskiy, M V Belous, V G Permyakov, V M Yashnil, "Electrophysical properties and phase composition of thin, cathode-sputtered Tantalum films," Fiz. metal. metalloved., Vol. 33 (3), pp. 564-570, 1972.

51. Part of work done by Neme Nnolim, Doctoral candidate, Materials Science and Engineering, New Jersey Institute of Technology, Newark, New Jersey, 2000.

52. Sungmin Maeng, Dr Lisa Axe, Dr Trevor Tyson, "Characterization of Gun-barrel Steel Corrosion in 37.8 % Hydrochloric acid with different exposure times," to be published, 2000.

53. D W Matson, M D Mertz, E D McClanahan, "Factors affecting tantalum deposition," *Journal of Vacuum Science and Technology*, Vol. A 10 (4), Jul/Aug. 1992, pp. 1791-1796.

54. Newton Schwartz, W A Reed, P Polash, Mildred H Reed, " Temperature coefficient of resistance of beta tantalum films and mixtures with bcc tantalum," *Thin Solid Films*, Vol. 14, 1972, pp. 333-347.

55. Dean W Matson, E D McClanahan, S Lee, J P Rice, D Windover, "Effect of sputtering parameters on tantalum coatings for gun-bore applications," Technical report ARCCB-TR-00014, US Army Armament Research Development Center, Aug. 2000.

56. E Collobert, Y Chouan, "A new hypothesis about sputtered tantalum," *Thin Solid Films*, Vol. 55, 1978, pp. L 15- L 16.

57. Keith Wagner, Sr. Materials Scientist, RG Lee Group, personal email dtd June 27th, 2001.

58. Personal conversation with Dr S L Lee, Bennet Labs, Dec. 2000.

59. Sheigehiko Sato,Tadahisa Inquee, Hajme Susaki, "Thermal oxidation of β- Ta below 500 °C," *Thin Solid Films*, Vol. 86, 1981, pp. 21-50.

60. Harold Basseches, " The oxidation of sputtered ta films," *Journal of Electrochemical Society*, Vol. 109, no. 6, 1962, pp. 475-479.

61. C A Streidel, D Gerstenberg, " Thermal oxidation of sputtered Ta thin films between 100 and 525 °C", *Journal of Applied Physics*, Vol. 40, no. 9, 1969, pp. 3828-3835.

62. D M Mattox, G J Kominak, " Structure modification by ion bombardment during deposition," *The Journal of Vacuum Science & Technology*, Vol. 9, 1971, pp. 528-532.

63. Robert E Reed, Reza Abbascian, *Physical Metallugy Principles*, PWS Publishing Company, 3rd Editon, 1994 and references mentioned therein.

64. Samples prepared by Dr Paul Cote, Benet Laboratory, Watervilet, NY.

65. Part of work done by Anamika Patel, Bhavin Shah, Dr Marek Sosnowski, Ion Beam and Sputter Lab, New Jersey Institute of Technology, Newark, NJ.